Contributions from California Coastal-Zone Surface Fluxes to Heavy Coastal Precipitation: A CALJET Case Study during the Strong El Niño of 1998

P. OLA G. PERSSON

Cooperative Institute for Research in Environmental Sciences and NOAA/Environmental Technology Laboratory, Boulder, Colorado

P. J. NEIMAN

NOAA/Environmental Technology Laboratory, Boulder, Colorado

B. WALTER

NorthWest Research Associates, Bellevue, Washington

J.-W. BAO AND F. M. RALPH

NOAA/Environmental Technology Laboratory, Boulder, Colorado

(Manuscript received 11 December 2003, in final form 7 July 2004)

ABSTRACT

Analysis of the case of 3 February 1998, using an extensive observational system in the California Bight during an El Niño winter, has revealed that surface sensible and latent heat fluxes within 150 km of the shore contributed substantially to the destabilization of air that subsequently produced strong convection and flooding along the coast. Aircraft, dropsonde, and satellite observations gathered offshore documented the sea surface temperatures (SSTs), surface fluxes, stratification, and frontal structures. These were used to extrapolate the effects of the fluxes on the warm-sector, boundary layer air ahead of a secondary cold front as this air moved toward the coast. The extrapolated structure was then validated in detail with nearshore aircraft, wind profiler, sounding, and buoy observations of the frontal convection along the coast, and the trajectory transformations were confirmed with a model simulation. The results show that the surface fluxes increased CAPE by about 26% such that the nearshore boundary layer values of 491 J kg^{-1} were near the upper end of those observed for cool-season California thunderstorms.

The increased CAPE due to upward sensible and latent heat fluxes was a result of the anomalously warm coastal SSTs (+1°–3°C) typical of strong El Niño events. Applications of the extrapolation method using a surface flux parameterization scheme and different SSTs suggested that convective destabilization due to nearshore surface fluxes may only occur during El Niño years when positive coastal SST anomalies are present. The fluxes may have no effect or a stabilizing effect during non–El Niño years, characterized by zero or negative coastal SST anomalies. In short, during strong El Niños, it appears that the associated coastal SST anomalies serve to further intensify the already anomalously strong storms in southern California, thus contributing to the increased flooding. This modulating effect by El Niño–Southern Oscillation (ENSO) of a mesoscale process has not been considered before in attempts at assessing the impacts of ENSO on U.S. west coast precipitation.

1. Introduction

Surface fluxes of sensible heat, moisture, and momentum over the oceans have long been thought to play a significant role in the modulation of the evolution and precipitation processes of maritime extratropical cyclones. The surface fluxes of heat and moisture have especially been thought to be an important source of energy for the development and sustenance of the precipitation. Specifically, the surface moisture flux provides a direct source of the moisture needed for precipitation, while the sensible heat flux can affect the stability of the storm environment, thereby modulating the precipitation process and amount.

Various studies, most relying on numerical models, have shown that the degree to which surface sensible heat and moisture fluxes affect storm evolution and precipitation depends on the location and timing of these fluxes relative to the cyclone and its associated

---

Corresponding author address: Dr. Ola Persson, CIRES/NOAA/ETL, R/ET7, 325 Broadway, Boulder, CO 80305.
E-mail: opersson@cires.colorado.edu

© 2005 American Meteorological Society

structures. Surface heat and moisture fluxes during the rapid deepening stages of the storms have produced only modest or no impacts on the storm development and precipitation (Kuo and Reed 1988; Kuo et al. 1991; Reed and Simmons 1991; Kristjánsson and Thorsteinsson 1995), while fluxes occurring before the rapid deepening stage produced larger impacts (Reed and Albright 1986; Kuo et al. 1991; Zhang et al. 1999; Gyakum and Danielson 2000). Using observational analyses, Reed and Albright (1986) and Gyakum and Danielson (2000) hypothesized that the large surface heat and moisture fluxes well in advance of developing Pacific cyclones, and before the rapid deepening stage, preconditioned the near-surface environment to the extent that explosive deepening occurred. Using an adjoint model on an idealized maritime cyclone, Langland et al. (1995) showed that surface sensible heat fluxes in the warm sector just ahead of the cold front produced the main impact on the cyclone evolution. Presumably, this was because the low-level jet (LLJ) ahead of the surface cold front is a principal means of inflow to developing cyclones (Wernli 1997).

In addition, the magnitude and even the sign of the impact depends on the relative temperatures of the ocean and the atmosphere. In one simulation of Langland et al. (1995), the surface sensible heat fluxes suppressed the cyclone evolution because they were downward due to the relatively warm southerly flow in the LLJ region passing over cooler waters typical of the North Pacific Ocean. In the simulations of Kuo et al. (1991), the warm sea surface temperatures (SSTs) of the Gulf Stream in the western Atlantic Ocean enhanced the development of the cyclones and their attendant precipitation. Hence, storms of comparable magnitude and thermal characteristics will be impacted differently over different oceanic regions. In an extreme case, Giordani and Caniaux (2001) showed that significant changes occurred in a developing, open-ocean storm passing over the strong 12°C SST gradient in the northwest Atlantic Ocean. Within 7 h of entering the warmer waters, the central pressure of the simulated storm was 11 mb deeper when compared to a simulation with spatially constant cold SSTs, and the track of the low deviated as well. In addition, the total precipitation in the case with the SST gradient was 66% greater, which was in large part due to the nearly threefold increase in the convective precipitation. These significant differences were due to the replacement of the significant downward sensible and latent heat flux in the warm sector with a near-zero heat flux and the increase in the baroclinicity due to an increase in the warm-air advection as the storm entered the warmer waters in the case with the SST gradient.

The SST can vary temporally as well as spatially, usually occurring on much longer time scales than that of the individual storms, thereby modulating the surface heat flux effect on the cyclones. A well-known example of temporal SST changes is that occurring with the El Niño–Southern Oscillation (ENSO). During the warm or El Niño phase of a strong ENSO, such as what occurred in 1982/83 and again in 1997/98, observations have shown that the SSTs in the central extratropical Pacific Ocean are anomalously cold, while the SSTs within 300 km of the California coast are anomalously warm (e.g., Namias and Cayan 1981; Lau 1997). Experiments with global circulation models (GCMs) have shown that these SST anomalies are due to the "atmospheric bridge" mechanism (Alexander 1990; Lau and Nath 1996). That is, they are produced through sensible and latent heat fluxes over the North Pacific Ocean associated with the anomalous extratropical atmospheric circulation, which, in turn, is generated by the tropical Pacific SST anomalies associated with ENSO. The positive SST anomaly along the California coast is only partially captured by the simple one-dimensional ocean mixed-layer representations in these experiments, suggesting that oceanic processes such as horizontal advection, upwelling, and coastally trapped waves are also necessary to produce the observed coastal anomalies (Lau and Nath 2001). Hence, if the coastal surface sensible heat and moisture fluxes are important for the development of an individual storm and its precipitation, one might expect a different impact during a strong, warm ENSO phase compared to other ENSO phases.

The California Land-falling Jets Experiment (CALJET; Ralph et al. 1999) conducted its field program over the coastal and offshore waters of California during the strong, warm ENSO phase in January and February 1998. This paper presents the case of 3 February 1998, for which the observed surface sensible and latent heat fluxes within 150 km of the shore within a prefrontal, moderate LLJ are shown to contribute significantly to the destabilization of the air just before it is lifted by the advancing cold front and the steep coastal terrain. As the air ascended, deep convection and intense precipitation occurred, resulting in significant coastal flooding. A bulk surface flux parameterization is used to extend the results to suggest that the coastal fluxes only enhance the coastal precipitation during years with anomalously warm SSTs (El Niño years) and may even help suppress coastal convection during years of more normal colder SSTs. This study builds upon a previous detailed diagnosis of the frontal structures and orographic effects in this same event presented by Neiman et al. (2004).

Section 2 briefly describes the measurements available for this study, and section 3 uses the observations to discuss the synoptic and mesoscale structure of this storm system. Section 4 describes the flux measurements and shows the impact of the surface fluxes on the coastal stability. In section 5, the output of a simulation of this case is examined to show that the observational assessments of the air trajectories and modifications are reasonable. In section 6, we generalize the results of section 4 to non–El Niño years and discuss how they fit

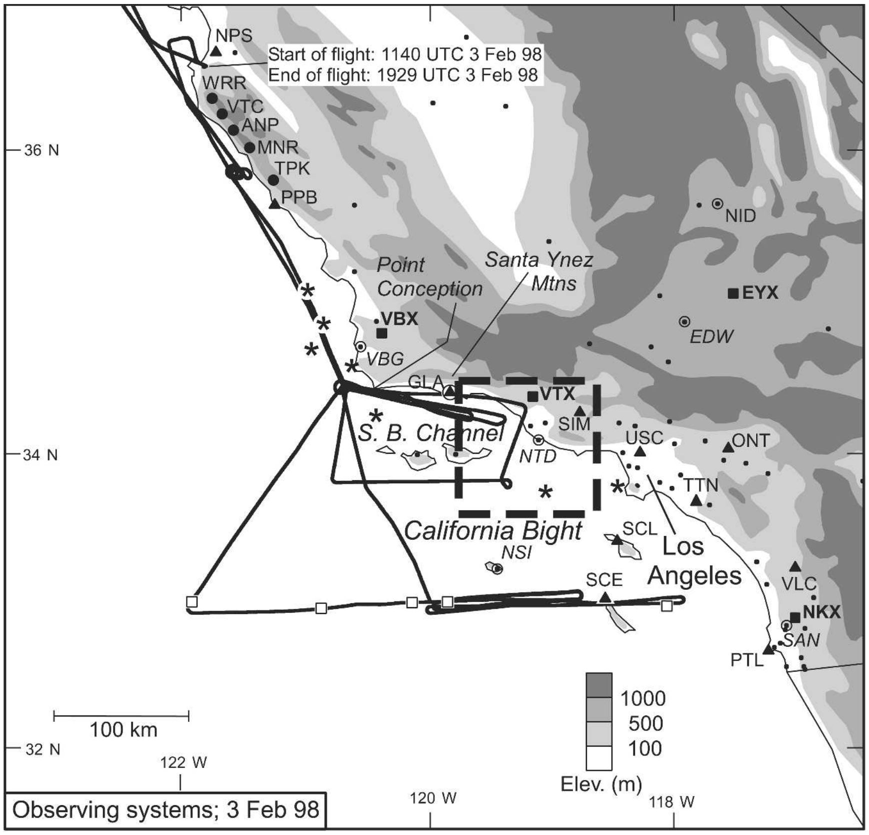
NPS
Start of flight: 1140 UTC 3 Feb 98
End of flight: 1929 UTC 3 Feb 98
WRR
VTC
ANP
MNR
TPK
PPB
36 N
NID
Point Conception
Santa Ynez Mtns
EYX
VBX
EDW
VBG
GLA
VTX
SIM
S. B. Channel
USC
ONT
34 N
NTD
TTN
California Bight
SCL
Los Angeles
NSI
SCE
VLC
NKX
SAN
PTL
1000
500
100
Elev. (m)
100 km
32 N
122 W
120 W
118 W
Observing systems; 3 Feb 98

FIG. 1. Terrain base map of southern California showing the locations of key observing systems (▲ = wind profilers; ■ = operational WSR-88Ds; ○ = rawinsondes; — = P-3 flight track; □ = P-3 dropsondes; * = moored buoys; ● = METAR (aviation routine weather reports) and RAWS surface sites; • = ALERT rain gauges). Only five ALERT rain gauge sites within the domain are shown and labeled; all ALERT sites with usable data are marked in Fig. 5 of Neiman et al. (2004). The bold, dashed box shows the area used in the dual-Doppler analysis of Fig. 10. "S. B. Channel" stands for the Santa Barbara Channel.

with current knowledge of ENSO-modulated effects on southern California precipitation. Section 7 provides a brief summary and some concluding remarks.

2. Observational platforms

The CALJET observational network in the California Bight region of southern California included both research and operational platforms (Fig. 1). The research platforms consisted of the National Oceanic and Atmospheric Administration (NOAA) WP-3D research aircraft (referred to as the P-3), an array of surface stations and 915-MHz wind profilers (most owned and operated by NOAA's Environmental Technology Laboratory) near the coast and on offshore islands, and special rawinsonde launches at Pt. Mugu (NTD), San Nicolas Island (NSI), and Goleta (GLA). The profiler winds were corrected with the measured vertical velocity component (Wuertz et al. 1988). The profiler, rawinsonde, and surface data collected at GLA are of particular importance to this study. The P-3 aircraft collected in situ measurements, data from a lower-fuselage (C band) radar and a Doppler tail (X band) radar, and dropsonde data. The instruments for collecting the in situ data are described by Friehe et al. (1986), Friehe and Khelif (1992), and Khelif et al. (1999). Jorgensen et al. (1983, 2003) describe the characteristics of the airborne radars. On 3 February, the P-3 aircraft flew between 1140 and 1929 UTC along the track shown in Fig. 1. It made measurements in the Santa Barbara Channel near GLA between 1230 and 1300 UTC, followed by a dropsonde cross section and flux stacks about 140 km farther south between 1330 and 1600 UTC. It then returned to the Santa Barbara Channel region between 1630 and 1800 UTC.

The operational platforms used in this study included the National Weather Service Next-Generation Weather Radars (NEXRADs) at Vandenberg (VBX), Ventura (VTX), and San Diego (NKX) and the Vandenberg (VBG) and San Diego (SAN) synoptic rawinsonde stations. Ralph et al. (1999, 2003) and Neiman et al. (2002, 2004) provide further descriptions of the observational network.

3. Synoptic and mesoscale structure

For the storm of 2–3 February 1998, phasing of a surface baroclinic zone with an upper-level circulation center led to cyclogenesis roughly 1000 km offshore (Persson et al. 1999; Ralph et al. 2003; Neiman et al. 2004). The offshore storm (Fig. 2a) had a complex mesoscale structure and an LLJ region containing winds over 40 m s^{-1} near 1 km in altitude. Already at 1200 UTC 2 February, the system consisted of a primary surface cold front with a secondary cold front to its west (Neiman et al. 2004).

The distributions of the SST and the SST anomalies are important for the understanding of the impact of the surface fluxes in this case. The 9-km resolution SSTs shown in Fig. 2b were obtained from daytime and nighttime measurements in cloud-free areas by the Advanced Very High Resolution Radiometer (AVHRR) on the NOAA polar-orbiting satellites and averaged over the 8 days beginning 1 February 1998. The SST anomalies for the same time period have a 50-km resolution and were obtained from NOAA/National Environmental Satellite, Data, and Information Service (NESDIS), who computed them from the nighttime-only AVHRR SST fields. The SST field shown in Fig. 2b has been validated at a few spot locations with downward-looking precision radiation thermometer (PRT-5) and airborne expendable bathythermograph (AXBT) measurements from the P-3 aircraft on 3 and 7 February. Those from 3 February are shown in Table 1 and discussed in section 4. At 1200 UTC 2 February, both frontal features are located over waters with near-normal SSTs (Fig. 2b). Farther offshore, the SSTs are significantly (1°–3°C) below normal, while along the U.S. West Coast they are 1°–3°C above normal. The positive anomaly represents the absence of the typical cold, upwelling waters generally found along the U.S. West Coast. At this time, a tongue of slightly warmer water can be found along the coast in the California Bight. The SST anomaly field during February 1998 is typical of a strong El Niño winter [compare to Fig. 2 of Lau (1997)].

The airflow in the California Bight is influenced both by the shape of the bight and by the surrounding terrain (see Fig. 1). The Santa Ynez Mountains just north of GLA form a steep, narrow wall rising up to 1000 m above the ocean. Individual peaks along these mountains reach 1310 m. The San Rafael Mountains just to the north of the Santa Ynez range have a relatively uniform height of 1500 m with peaks to 2000 m.

As the storm system approached the southern California coast on 3 February, complex interactions occurred between the coastal orography in the California Bight region and the landfalling storm, as described by Neiman et al. (2004). A prefrontal squall line and the primary cold front produced the initial heavy precipitation. The secondary cold front produced brief but very intense precipitation in the coastal mountains along the northern shore of the California Bight. In some areas of the southern California coastal mountains, 24-h precipitation totals from this storm exceeded 300 mm (12 in.), resulting in flooding and mudslides. The storm also forced the closure of Los Angeles International Airport (LAX). At 1500 UTC on 3 February 1998, the primary cold front of this system was over Los Angeles, while the secondary cold front had just made landfall near Pt. Conception (Fig. 3). The *Geostationary Operational Environmental Satellite-10* (*GOES-10*) infrared image shows that the deeper clouds of the comma-cloud tail are mainly located between the primary and secondary cold fronts and suggests that the fronts extend well south of 25°N and that the low-level air parcel trajectories have a subtropical origin. The secondary front is the main focus of this study. Discussions of the primary front will be limited to those necessary to explain the environment for the secondary front. More details of the primary front and the complex interactions of the landfalling fronts with the coastal orography are presented by Neiman et al. (2004).

The sea level pressure and wind field analyses of buoy, aircraft, and wind profiler measurements show more details of the conditions near the primary and secondary fronts (Fig. 4). The analysis by Neiman et al. (2004), from which Fig. 4 is adapted, shows that the lower portion of the primary front near the coastal terrain has been retarded, leaving a low-level remnant primary front over the Channel Islands and the Santa Barbara Channel as the secondary front approaches from the west at 1500 UTC 3 February. South of the Channel Islands, the low-level airflow is southerly ahead of the secondary cold front, while it is more southeasterly to the east of the remnant low-level primary front in the Santa Barbara Channel. Hence, from the location of the low-level aircraft measurements (solid dot heads in Fig. 4) until it is turned near the northern coast of the bight, the presecondary frontal, low-level flow is parallel to the secondary front. The northwesterly low-level winds in tandem with the southwesterly midtropospheric cloud-track winds just behind the secondary cold front (Fig. 3) show that the postsecondary front winds are backing with height, consistent with cold-air advection.

Figure 5 shows frontal analyses superimposed on NEXRAD images from VTX at 1502 and 1732 UTC. The frontal analyses are based on the various data sources available. The aircraft flight track in Fig. 5a is adjusted to the radar time based on a frontal phase velocity of 16.8 m s^{-1} from 200°, which was obtained from the movement of individual precipitation cells evident in the offshore region in the series of NEXRAD images. For Fig. 5b, to insure that the tracks not be

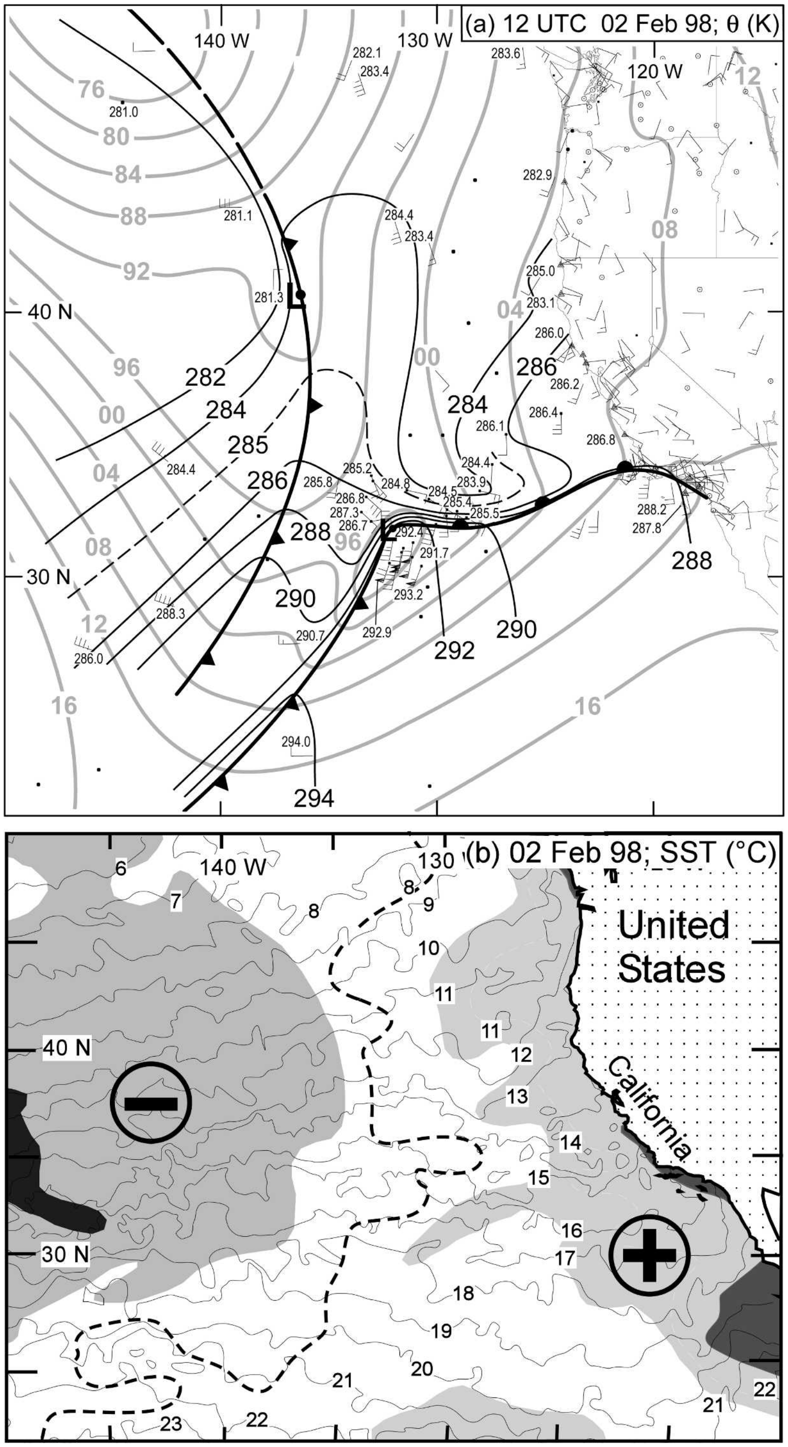
(a) 12 UTC 02 Feb 98; θ (K)
140 W
130 W
120 W
40 N
30 N
76
80
84
88
92
96
00
04
08
12
16
282
284
285
286
288
290
292
294
(b) 02 Feb 98; SST (°C)
140 W
130
40 N
30 N
United States
California
6
7
8
9
10
11
12
13
14
15
16
17
18
19
20
21
22
23

FIG. 2. (a) Analysis of sea level pressure (gray lines; mb) and near-surface potential temperature (black solid; K) at 1200 UTC 2 Feb 1998. Near-surface wind flags and potential temperature observations from buoys, ships of opportunity, and the NOAA P-3 aircraft are also shown. Wind flags are 25 m s^{-1}, full barbs are 5 m s^{-1}, and half barbs are 2.5 m s^{-1}. Standard frontal notation is used. (b) SST (solid lines; °C) and SST anomalies (shading) for 2 Feb 1998. SST anomaly magnitudes greater than 0.5°C (2.0°C) are shown by light (dark) shading, with positive anomalies to the right of the 0°C anomaly isopleth (heavy dashed line) and negative anomalies to the left (marked by symbols). Both (a) and (b) depict the same area but have different shapes because of different map projections.

TABLE 1. Mean values along the flux stack legs in the offshore warm sector of pressure (p), air temperature (T), mixing ratio (q), virtual potential temperature (θ_v), equivalent potential temperature (θ_e), wind speed (ws), wind direction (wd), latent heat flux (H_l), sensible heat flux (H_s), and stress (τ). The brackets indicate mean values, and "xs–xe" shows the starting and end points of the warm-sector portion of the legs in the time-to-space-adjusted cross-frontal direction. The two surface temperatures (T at 0-m height in rows 1 and 2) are given by an AXBT and the airborne downward-looking precision radiation thermometer (PRT-5), respectively, while the surface mixing ratio (q) is computed assuming saturated conditions for seawater.

Time	Height (MSL)	xs–xe	$\langle p\rangle$	$\langle T\rangle$	$\langle q\rangle$	$\langle\theta_v\rangle$	$\langle\theta_e\rangle$	⟨ws⟩	⟨wd⟩	H_l	H_s	τ
UTC	m	km	mb	°C	g kg^{-1}	K	K	m s^{-1}	degrees	W m^{-2}	W m^{-2}	N m^{-2}
1520:16 AXBT	0	96	—	15.73	—	—	—	—	—	—	—	—
1552:50–1557:00	0	69–98	993.6	15.8	11.17	291.4	320.9	0	—	—	—	—
1552:50–1557:00	66	69–98	985.7	14.9	9.47	290.9	316	13.4	198	32.1	12.1	0.09
1531:00–1535:18	285	75–102	960.5	13.15	9.09	291.2	315.4	14.8	197	42.0	−6.0	0.05
1519:00–1524:00	427	70–104	944.3	12.29	8.89	291.7	315.4	15.6	195	113.6	−47.0	0.19
1453:00–1457:00	590	76–102	926.5	11.22	8.38	292.1	314.6	16.6	198	2.5	−12.1	0.06
1446:00–1450:00	1154	73–102	866.6	8.1	6.95	294.2	313.2	13.9	194	32.0	6.0	−0.03

shown over land, the adjustment is made with the east–west component of the above-phase velocity, that is, 6.0 m s^{-1} from 270°. If the full phase velocity had been used, the 1635–1710 UTC aircraft pass through the front would erroneously appear as if it had occurred over land in an area where no radar reflectivities from VTX exist because of the radar-beam occultation by the terrain.

Figure 5a shows that the offshore sampling by the P-3 was done between 1430 and 1620 UTC primarily ahead of the secondary front. The altitudes of the five legs of this offshore "flux stack" are given in Table 1 and were

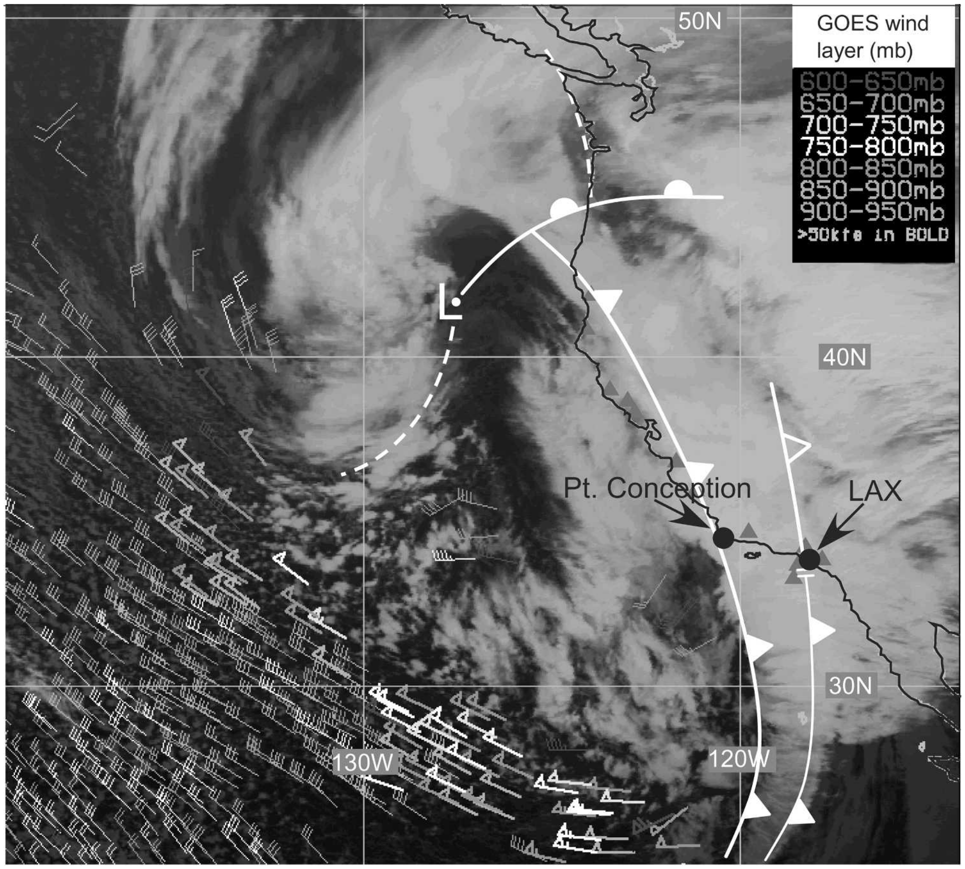

FIG. 3. GOES infrared image and cloud-track winds below 600 mb (flags and barbs are as in Fig. 2) at 1500 UTC 3 Feb 1998. The primary and secondary cold fronts in the California Bight are shown, with the open symbol indicating the primary front aloft. A bent-back front is dashed. The heights of the cloud-track winds are coded by shading. CALJET coastal wind profiler sites (see Fig. 1) are shown as filled triangles.

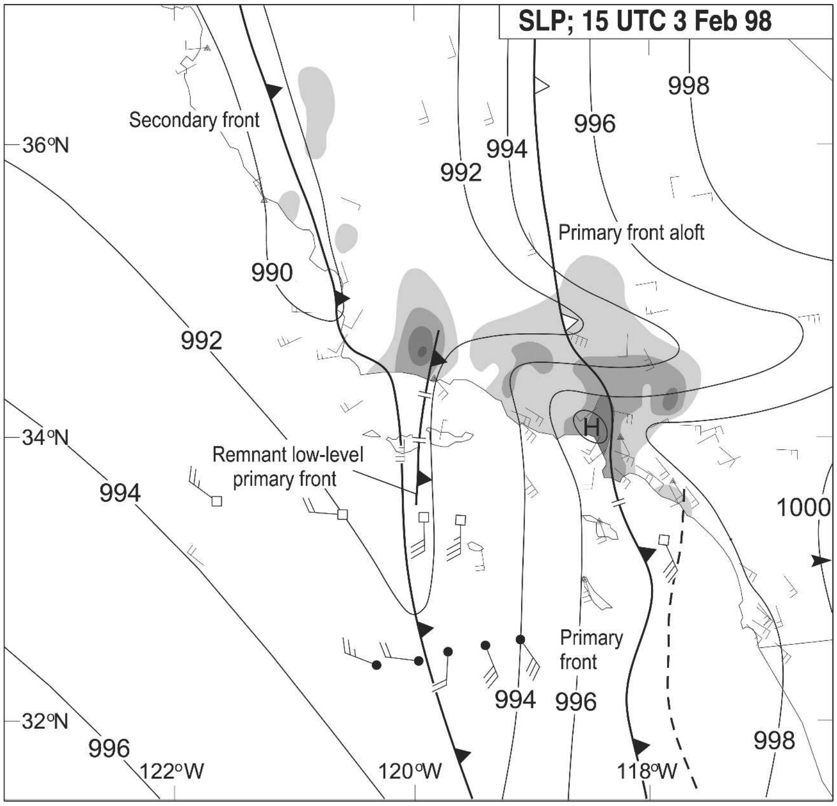

FIG. 4. Mesoscale sea level pressure analysis and low-level wind data at 1500 UTC 3 Feb 1998. Wind flags and barbs are as in Fig. 2. The land-based observations are from METAR sites (no vector heads) and profiler sites (triangle vector heads). The ocean-based observations are from ships and buoys (no vector heads). Winds with open-square heads and solid-dot heads portray time-to-space-adjusted P-3 near-surface dropsonde data and low-level (~60 m MSL) flight-level data, respectively. Open frontal symbols portray fronts above the surface. The bold dashed line defines the prefrontal squall line. Gray shading represents the 3-h accumulated rainfall centered on the analysis time (light: 12–24 mm; medium: 24–36 mm; darker: 36–48 mm; darkest: >48 mm).

chosen in real time so the lowest height is in the constant flux layer [lowest 10% of the planetary boundary layer (PBL); e.g., see Garratt (1992)] and the top two legs bracketed the top of the PBL. The legs were done in descending order from 1154 m near 1445 UTC to 66 m near 1555 UTC, with the last leg crossing the cold front near 1557 UTC. At the time of this offshore sampling, only very weak precipitation was occurring offshore near the aircraft, while the precipitation intensity (34–40 dBZ) near the coast just west of GLA was beginning to increase as the advancing secondary cold front merged with the nearly stationary, remnant, low-level, primary cold front (Neiman et al. 2004).

During two 7-min periods (1647–1655 and 1742–1752 UTC) approximately 2 h later, the P-3 sampled nearly the same prefrontal air but now at the northern end of the bight near the steep coastal terrain. During the nearshore flight legs at altitudes of about 275 and 1570 m, most of the low-level sampling was done in the postfrontal air because of flight safety concerns due to the proximity of the mountains. By these times, as represented by the 1732 UTC image (Fig. 5b), the precipitation intensity along the secondary cold front in the nearshore region had intensified by about 10–12 dBZ from that seen near 1502 UTC. The phase velocity of 16.8 m s^{-1} from 200° corresponds to this 120–150-km movement in 2–2.5 h of warm-sector air from the offshore to nearshore sampling locations.

Surface data collected at the GLA coastal site show the moderate precipitation rates associated with the primary cold frontal passage during the early part of 3 February and the more intense precipitation with the later secondary cold front between 1502 and 1732 UTC (Fig. 6). As the secondary cold front passed over GLA, it produced a surface 2-min average precipitation rate of 76 mm h^{-1}, and 24.3 mm of rain fell between 1600 and 1700 UTC. This heavy burst of precipitation falling on the ground already saturated by about 48 mm of precipitation from the primary front led to local flooding. Precipitation associated with the secondary front (i.e., after 1330 UTC) totaled 50 mm at a mountain station just north of GLA, showing a 25% increase over

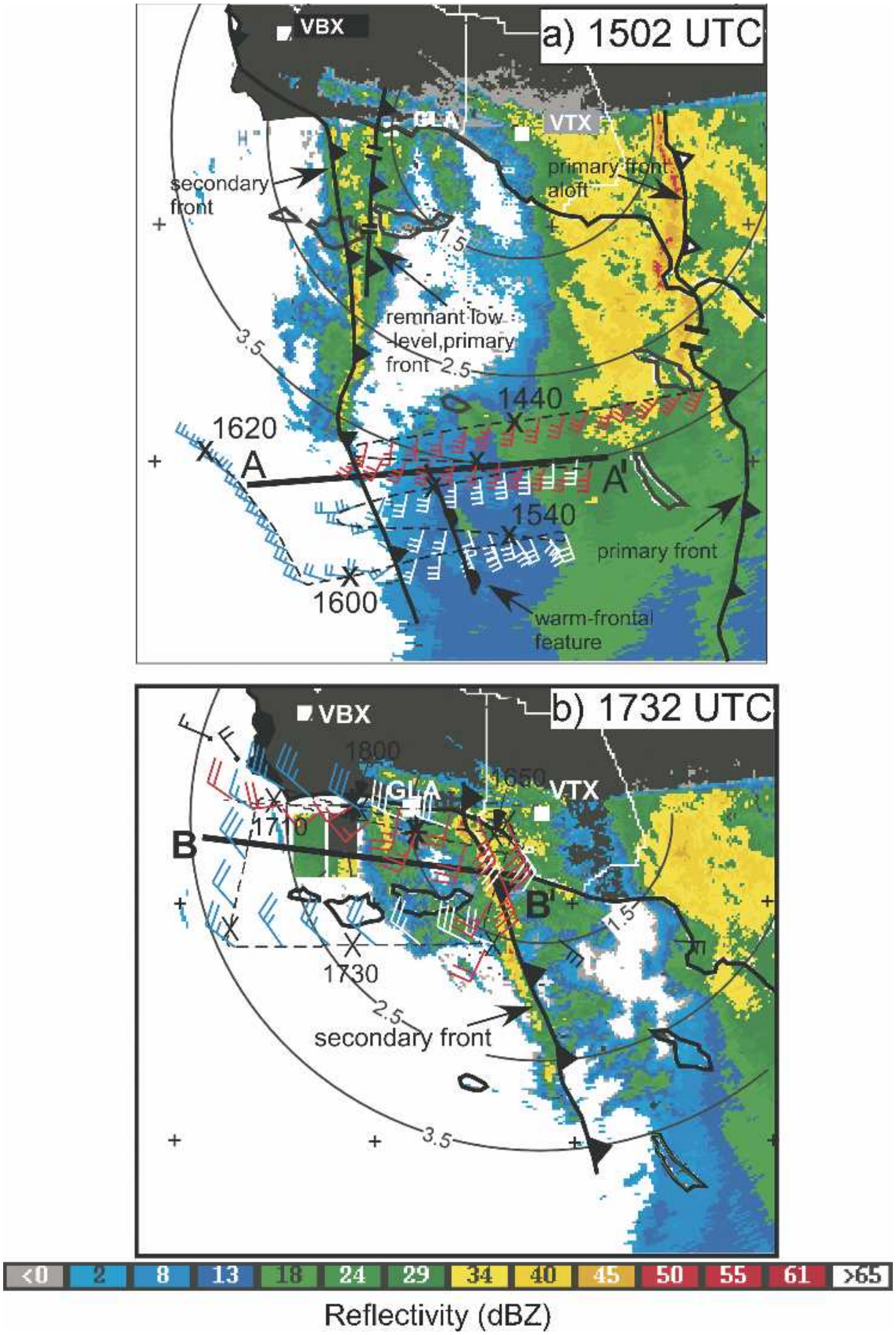
a) 1502 UTC
VBX
GLA
VTX
primary front aloft
secondary front
1.5
remnant low level, primary front
2.5
3.5
1440
1620
A
A'
1540
primary front
1600
warm-frontal feature
b) 1732 UTC
VBX
1800
GLA
1650
VTX
1710
B
B'
1.5
1730
2.5
secondary front
3.5
<0
2
8
13
18
24
29
34
40
45
50
55
61
>65
Reflectivity (dBZ)

FIG. 5. Radar reflectivity (dB*Z*; 0.5° elevation scans) from the NEXRAD at VTX at (a) 1502 and (b) 1732 UTC 3 Feb, overlaid with the surface frontal analyses. The time-to-space-converted P-3 tracks (dashed) were computed using a velocity of (a) 16.8 $\mathrm{m\,s^{-1}}$ from 200° and (b) 6 $\mathrm{m\,s^{-1}}$ from 270°. See text for clarification. The bold lines A–A′ and B–B′ show the locations of the cross sections in Figs. 7 and 8, respectively. Time hacks (X) along the flight tracks are every 20 min in (a) and 10 min in (b); labels at selected time hacks are times (UTC) on 3 Feb 1998. The selected wind barbs are red for aircraft altitudes above 500 m and blue or white for those below. The black ones in (b) are from buoys. Wind barbs are as in Fig. 2.

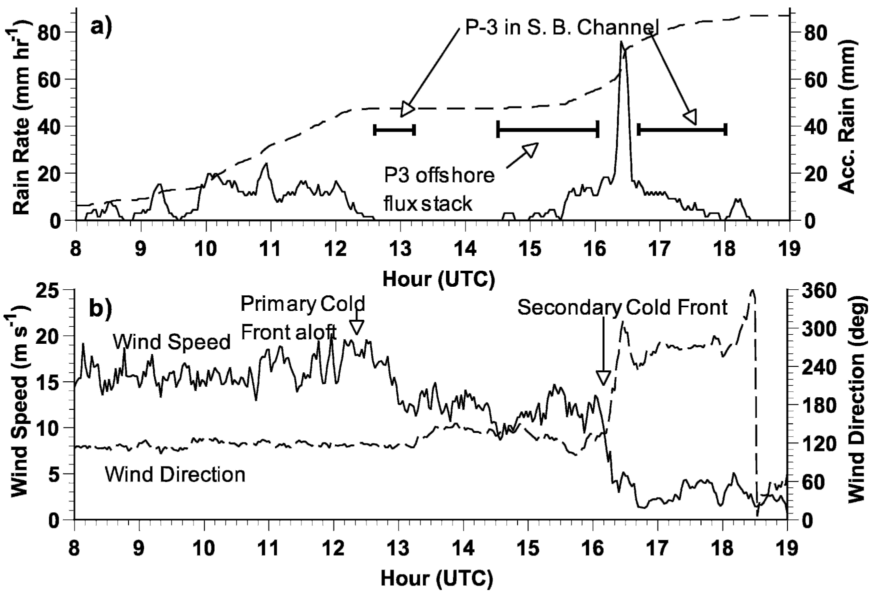

FIG. 6. Surface observations at the GLA wind profiler for 3 Feb 1998. Shown are (a) 2-min average rain rate (solid) and accumulated rainfall (dashed), and (b) wind speed (solid) and direction (dashed). The times when the P-3 aircraft was located in the Santa Barbara Channel and offshore are marked in (a).

the 40 mm of precipitation at GLA. Neiman et al. (2002) show that the rain rate in the coastal mountains is directly proportional to the strength of the cross-shore wind component near a height of 1 km, which in this case was between 15 and 20 m s^{-1}. The wind direction was steadily from the southeast before and after the passage of the primary front aloft (Fig. 6b), veering to due westerly only after the passage of the secondary cold front. The surface wind speed was 15–18 m s^{-1} ahead of the primary front aloft, a moderate 10–14 m s^{-1} before the passage of the secondary cold front, dropping off to less than 5 m s^{-1} afterward.

Cross sections along the lines A–A′ at 1502 UTC and B−B′ at 1732 UTC in Figs. 5a and 5b show the vertical structure of the secondary cold front offshore and nearshore (Figs. 7 and 8), respectively. These cross sections were constructed using the in situ aircraft data at altitudes below the top sampling height for each area and the relevant offshore dropsondes, dropped between 1335 and 1359 UTC at the locations shown in Fig. 1, at higher altitudes. Hence, above about 1700 m (i.e., above the highest flight leg in the cross sections), the nearshore cross section has the same dropsonde data as the offshore cross section. All data were time adjusted

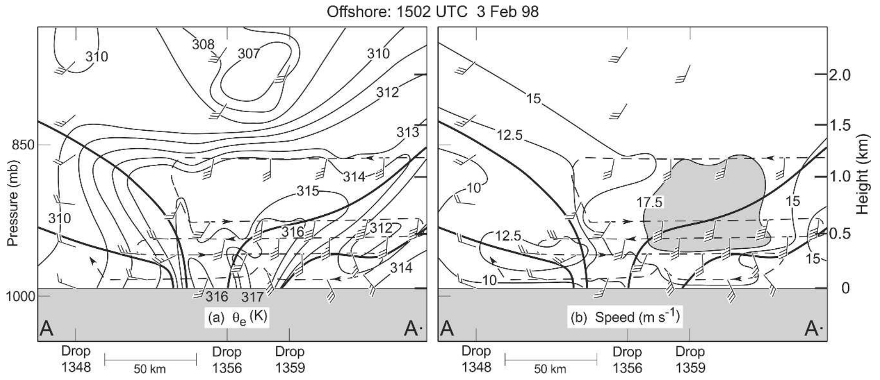

FIG. 7. Offshore cross sections of (a) θ_e (K) and (b) wind speed (m s^{-1}; shading >17.5 m s^{-1}) along the line marked A–A′ in Fig. 5a. The analyses used aircraft data from 1440 to 1605 UTC and the marked dropsondes above the highest aircraft data. Also shown are the wind barbs as in Fig. 2 and aircraft tracks (dashed). The frontal zones are encompassed within the heavy solid lines. A velocity of 16.8 m s^{-1} from 200° was used in the time-to-space conversion of the aircraft data.

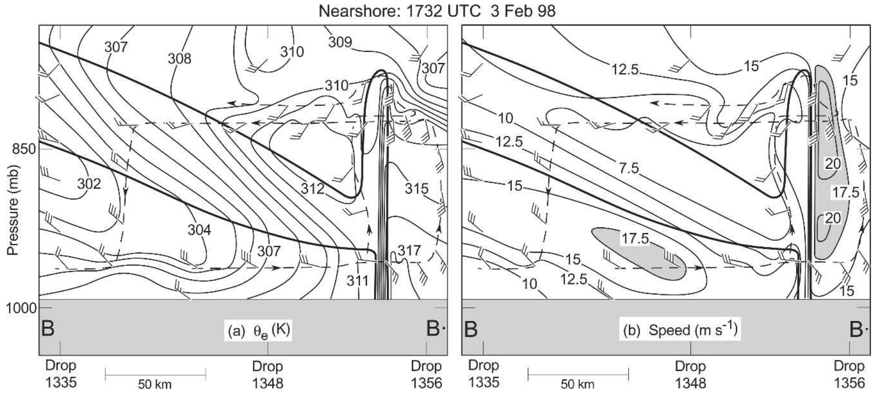

FIG. 8. As in Fig. 7, but along the nearshore line marked B–B′ in Fig. 5b. In addition to aircraft and droposonde data, buoy data were also used. In (b), the analysis included the use of wind profiler data from Goleta (not shown). A velocity of 6.0 m s^{-1} from 270° was used in the time-to-space conversion.

and projected onto the cross sections before the analysis was done. In addition, wind profiler data from GLA were used to refine the isotach analysis in the nearshore cross section (Fig. 8b). Using the same dropsonde data above 1700 m MSL for the nearshore and offshore cross sections is an advantage in this case because the differences between the cross sections thereby highlight the differences in the boundary layer, which is the region of focus for this study.

The offshore analyses of equivalent potential temperature [θ_e; computed from the relations of Bolton (1980)] and isotachs reveal a narrow warm-sector region between a shallow warm-frontal-like feature to the east and the secondary cold front to the west (Fig. 7a). The presence of the secondary front is marked by the leading edge of a decrease of 3 K in θ_v (not shown), 6 K in θ_e, and 6 m s^{-1} in wind speed. The low-level wind direction veers by 90° across the cold front, from south-southwesterly to west-northwesterly. The cold front rises abruptly to about 910 mb (700 m) before the slope decreases. The warm-frontal feature is at the western edge of air that is slightly cooler and significantly drier than the warm sector, with θ_e values 2–5 K lower than in the warm sector. The depth of this cool/dry air extends to about 1.0–1.5 km 125 km to the east of the surface warm front. A low-level region of warm, moist air is located in the warm sector between the two fronts, with the highest θ_e air occurring in two smaller tongues, one in the warm sector just ahead of the surface cold front and a second along the western edge of the warm front. In the warm sector, the maximum θ_e is about 316 K. The wind direction backs 45° going from the warm sector into the cooler air to the east. Hence on the lowest leg, the warm sector is only about 25–30 km wide, but significantly wider at the higher legs. A southerly 17.5–20 m s^{-1} LLJ (shaded in Fig. 7b) is present just above the warm-frontal feature, extending into the warm sector ahead of the secondary cold front at a height of about 600 m.

In the 2–2.5 h between the offshore and nearshore measurements, the offshore bubble of warm, moist air in the warm sector advected toward the coast to the NNE, keeping just to the east of the secondary cold front. If applied for 2.25 h, the bulk phase velocity of 16.8 m s^{-1} from 200° moves the prefrontal bubble 136 km toward the NNE, arriving near the coast at about the same time as the aircraft did the nearshore sampling. This is illustrated schematically in Fig. 9. Note that this phase velocity is very close to the observed, offshore, warm-sector wind velocity.

To assess whether the offshore warm-sector air mass will be lifted by the cold front before the warm-sector air reaches the coast, we can compute the differential velocity of the warm-sector PBL and the cold front in the cross-frontal direction. Using the frontal phase velocity of 16.8 m s^{-1} from 200° yields an eastward component of 5.7 m s^{-1} while the mean eastward wind component on the three lowest legs in the boundary layer (427 m and below; see Table 1) is 4.1 m s^{-1}, yielding a frontal differential eastward velocity of 1.6 m s^{-1}. Hence, in 2.25 h, the cold front will encroach 13 km into the warm sector shown in Fig. 7, which is about half the width of the offshore warm sector. This simple calculation suggests that the eastern half of the warm sector will have the entire 2.25 h to be modified by the surface fluxes while the western half of the warm sector will have progressively less time the closer to the cold front. This calculation assumes constant boundary layer air velocity and frontal phase velocity (actually, constant relative velocity) and that our estimate of the frontal phase velocity is accurate. An error in the frontal phase speed of 1 m s^{-1} (6%) and in-phase direction of 5° will produce encroachments between 0 and 28 km, depending on the signs of the errors. Hence, our best estimate suggests that half of the offshore, warm-sector, boundary layer air is not lifted by the front in the time it took to reach the coast, but the uncertainty is such that none or all of it may have been lifted. However, the combi-

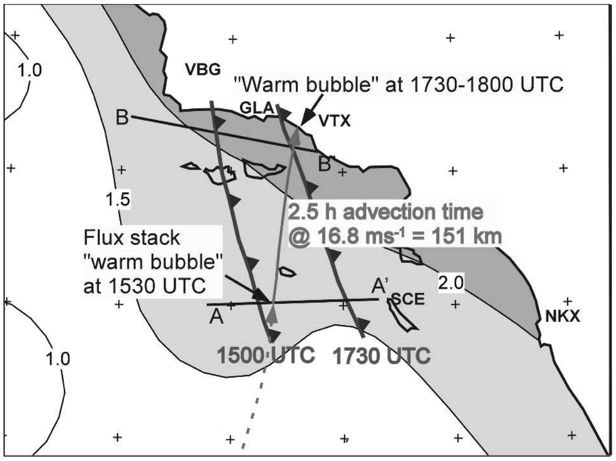

FIG. 9. Schematic of the parcel trajectory from the offshore cross section (A–A′) to the nearshore cross section (B–B′) at the north coast of the California Bight. The two heavy lines with frontal symbols represent the secondary cold front at 1500 and 1730 UTC, respectively. The isopleths show the SST anomaly (°C) for 2 Feb 1998, with the anomalies above +1.5°C (light shading) and +2.0°C (dark shading) highlighted.

nation of several facts suggests that, at most, only a part of the warm sector was lifted, so the nearshore sampling by the P-3 occurred in approximately the same air that was sampled offshore. These facts are 1) the front-parallel nature of the low-level, front-relative flow in the warm sector south of coastal blocking effects (shown by the dual-Doppler radar analysis later in this section), 2) the absence of significant upward motion away from the front in the warm sector (also shown later in this section), and 3) the close agreement between the extrapolated offshore and observed nearshore warm-sector thermodynamic structure (see section 4b). The numerical simulation results presented in section 5 provide further support for this assertion.

Figure 8a shows the nearshore θ_e analysis valid near 1730 UTC along the line B–B′ indicated in Fig. 5b. This analysis represents the nearshore environment after the merger of the secondary cold front with the low-level remnant of the primary cold front (Neiman et al. 2004). Compared to offshore, the nearshore bubble of high θ_e in the warm sector has increased by 1 K to 317 K. The GLA wind profiler data incorporated into Fig. 8b show that the prefrontal LLJ has increased by 1–2 m s^{-1}, has moved closer to the surface cold front, and has two centers, one near 600–700 m in altitude as offshore and one near 1200–1500 m. The wind direction in the lowest center is now from the southeast, rather than from the south-southwest, however. The leading edge of the cold front offshore was shallow and sloped in the absence of convection, whereas the leading edge of the front nearshore ~2.5 h later was more vertical, likely due to the development of the convective squall line along the front.

The flight leg at 1570 m from 1739 to 1751 UTC provides an opportunity to sample the nearshore warm-sector air using the tail radar data from the P-3 with a fore/aft scanning sequence (Jorgensen et al. 1996). The pseudo-dual-Doppler analysis of the radar data was similar to that described by Jorgensen et al. (2003), except that a single pulse-repetition frequency demanded manual unfolding of the radial velocities, the full scanning sequence produced a horizontal data spacing of ~1400 m, and the Doppler data were interpolated to Cartesian grids with a spacing of $\Delta x = \Delta y = 1.0$ km and $\Delta z = 0.25$ km, where the vertical levels were constructed relative to mean sea level. Corrections to the radial velocities for particle fall speeds were done as described by Jorgensen et al. (2003) assuming rain existed below 1.75 km and snow existed above 2.25 km, and using a linear fall velocity interpolation between these heights. The magnitudes of the fall velocity corrections were kept small by using data only from elevation angles between ±45°.

Figure 10 shows this flight leg together with the ground-relative airflow and radar reflectivity at 1.0-km altitude. Other diagnostic parameters that have been examined but are not shown include the vertical velocity, relative vorticity, and divergence fields. The presence of the cold front is marked by the strong NNW–SSE-oriented wind shift and line of heavy precipitation. The wind is from the S to SE at 15–22 m s^{-1} ahead of the front and from the W to SW at 7–12 m s^{-1} behind. Within about 25 km of the shore, the airflow ahead of the front at 1.0 km has a stronger easterly component than farther south, marking the seaward extent of the blocking effects of the coastal mountains. Hence, within 25 km of the shore, air arriving from the south accelerates toward the cold front, where it is lifted. As is typical for narrow cold-frontal rainbands (NCFRs), the alongfront precipitation is organized into precipitation cores and gap regions (e.g., Hobbs and Persson 1982; Wakimoto and Bosart 2000; Jorgensen et al. 2003).

The convergence at the cold front produces an updraft of nearly 6 m s^{-1} at a height of 2.5–3.0 km (Fig. 11a). Though weaker aloft, the updraft extends to above 6 km and is associated with significant precipitation to this height. Such a deep updraft is unusual for NCFRs and probably indicates some amount of free convection rather than just the forced convection typical of NCFRs (e.g., Hobbs and Persson 1982; Parsons 1992; Wakimoto and Bosart 2000). This would be consistent with a modest amount of convective available potential energy (CAPE) in this case (see section 4b). The strong ascent produces the heavy precipitation, with reflectivities over 46 dBZ evident at 1.0-km height down to the surface. The prefrontal LLJ of alongfront winds has two maxima, one of 17.5 m s^{-1} at 500 m (note wind barbs at the bottom edge of the data) and another of 20 m s^{-1} at 1.4 km (Fig. 11b), in agreement with the analysis shown in Fig. 8b. The lower one likely corresponds to the LLJ maximum observed offshore, as it has the same speed and height. The flow is southerly

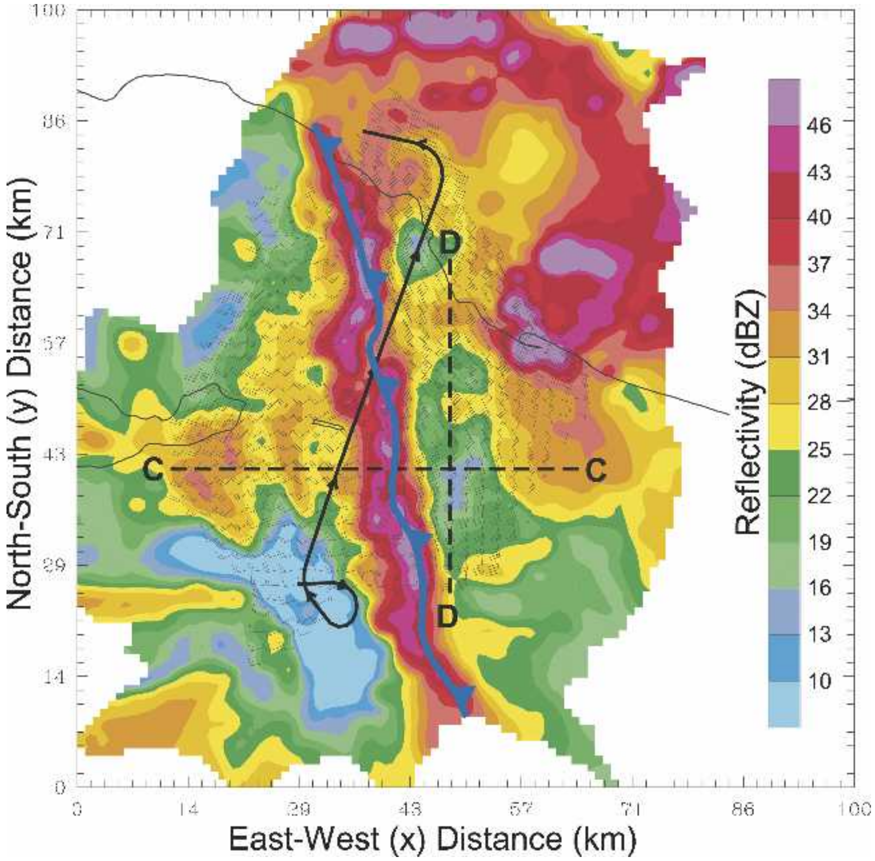

FIG. 10. Pseudo-dual-Doppler radar analyses from the NOAA P-3 tail radar at 1739–1751 UTC 3 Feb 1998, showing the horizontal fields of reflectivity (dBZ) and ground-relative horizontal winds (as in Fig. 2) at 1.0 km MSL. The location of the surface cold front (blue) is based primarily on the wind direction shear. The black dashed lines C–C′ and D–D′ mark the locations of the cross sections in Figs. 11 and 12, respectively. The P-3 flight track is portrayed as a bold black line. See Fig. 1 for the location of this analysis.

ahead of and above the cold front, with a slight easterly component below 700 m in the warm sector just ahead of the cold front. The frontal boundary in Fig. 11 was determined from the leading and top edge of the horizontal and vertical shear in Fig. 11b, respectively, and corresponds to the maximum vertical shear in the cross-frontal flow in Fig. 11a.

Figure 12 shows the in-section, ground-relative airflow (vectors) and the zonal-component isotachs in a north–south cross section in the warm sector, whose position is marked by the dashed line D–D′ in Fig. 10. The easterly component (i.e., $u < 0$ m s^{-1}) increases (u decreases) by 16 m s^{-1} from 25 km offshore ($y = 38$ km) to very close to the shore ($y = 63$ km) at an altitude of about 500 m. This wedge-shaped region of increase in the easterly flow slowly deepens from below 1 km near $y = 38$ km to an altitude of about 1.9 km near the shore, and likely represents the depth over which the terrain affects the southerly flow consistent with the orographic turning effects observed by Neiman et al. (2004). In contrast, the southerly flow generally only has much smaller variations of a few meters per second, with the exception of a local southerly wind maximum near $y = 38$, probably associated with the proximity of the precipitation core as noted by Wakimoto and Bosart (2000). The cross section shows no evidence for a thermodynamic blocking front feature lifting the boundary layer air arriving from the south. That is, while the coastal terrain deflects the air westward, as also observed in the case studied by Yu and Bond (2002), there is no evidence of an air mass with different thermodynamic characteristics trapped along the coastal terrain with coast-parallel convergence and lifting in the manner discussed by Bjerknes and Solberg (1921), Doyle (1997), and Garner (1999). In fact, the divergence field at 500-m height (not shown) shows no indication of a coast-parallel band of convergence, and subsidence is present in the lower levels within 12 km of the shore, perhaps caused by local flow around the Santa Monica Mountains.

Of primary significance is that the warm-sector PBL air remains near the surface but is accelerated westward

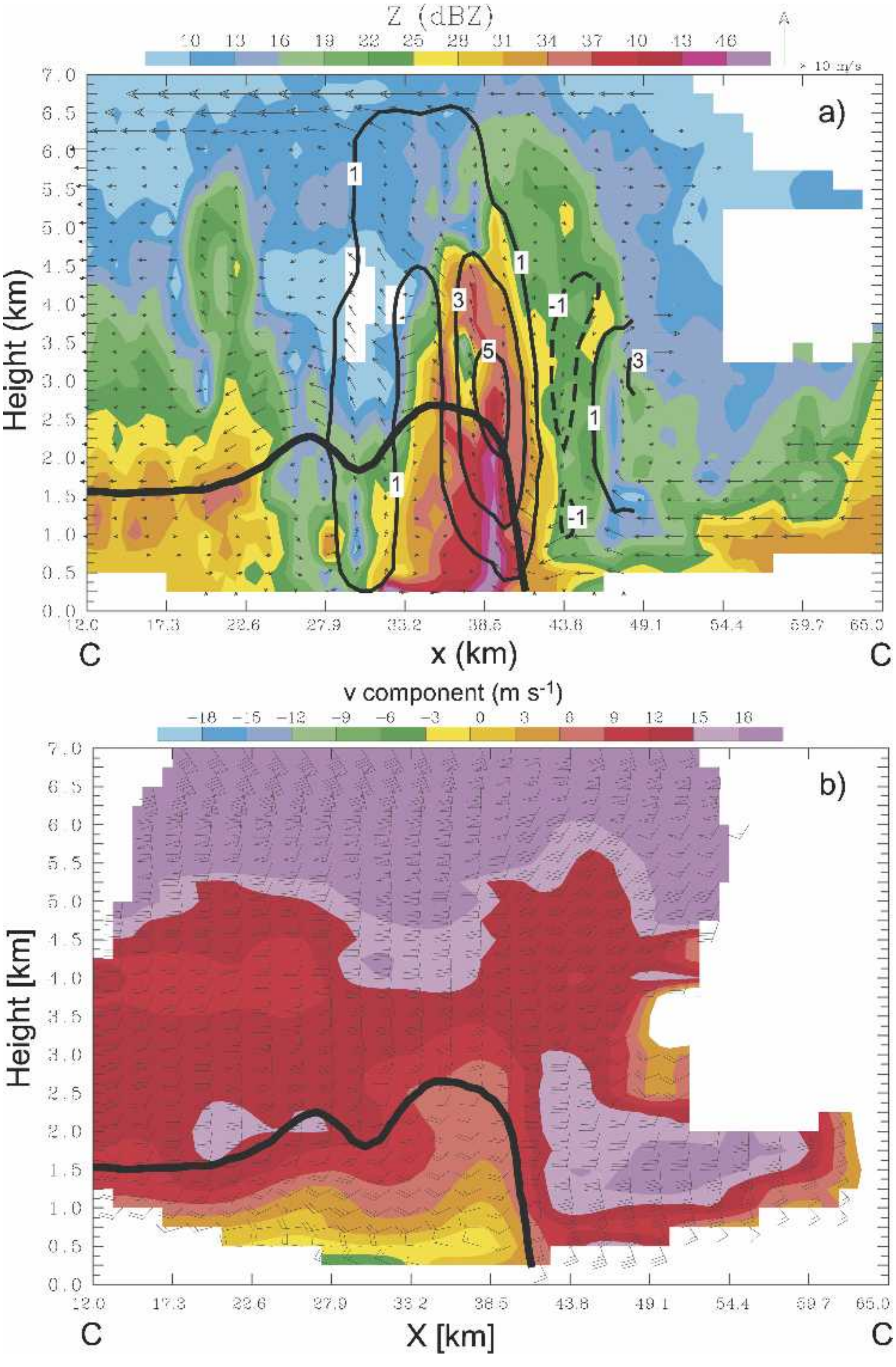

FIG. 11. Vertical cross sections along the cross-front line C–C′ in Fig. 10 showing (a) the radar reflectivity (color shading; dBZ), the vertical velocity (thin black lines, with negative values dashed; m s^{-1}), and the in-plane, front-relative wind vectors (scale upper right), and (b) the plane-perpendicular wind component (v) and the ground-relative winds (flags and barbs are as in Fig. 2). The bold curve shows the frontal boundary determined from the leading and top edge of the horizontal and vertical shear in (b), respectively, and corresponds to the maximum vertical shear in the cross-frontal flow in (a).

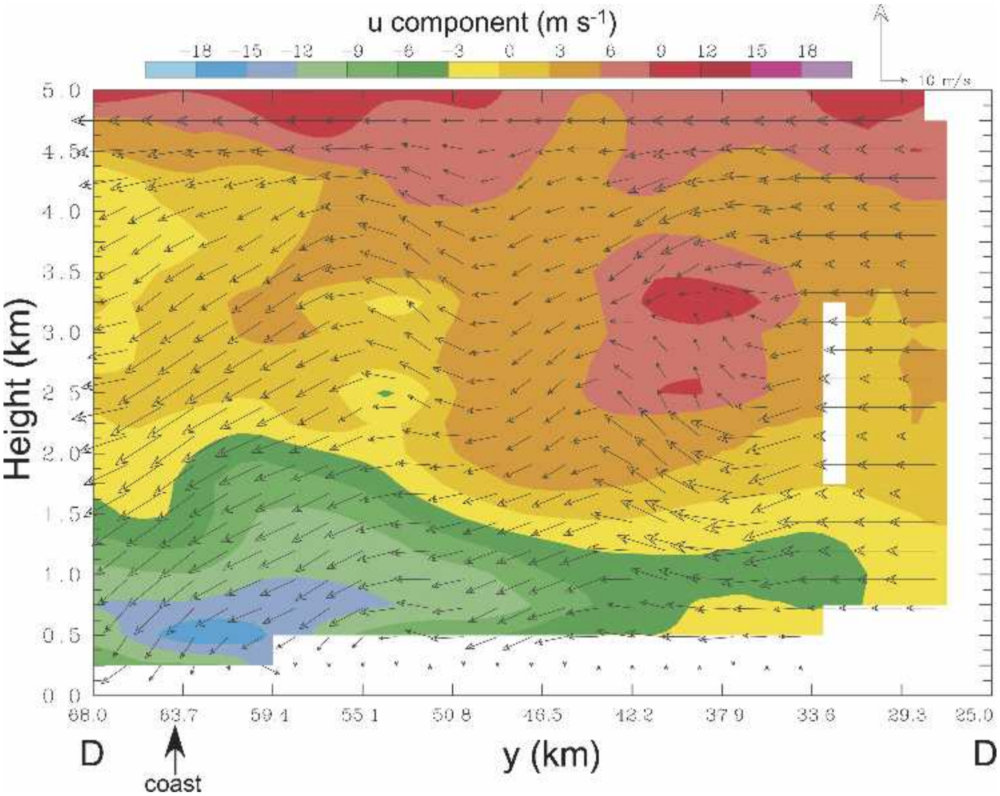

FIG. 12. North–south cross section along the line D–D′ in Fig. 10 showing in-plane, ground-relative wind vectors (scale upper right) and the plane-perpendicular wind component (u). The arrow at $y = 64$ km marks the location of the coastline.

toward the front. Hence, the parcels that are nearest the surface farther south tend to stay within the PBL until they are lifted at the front after having been turned toward the west by pressure-gradient forces established by topographical effects.

4. Sea surface fluxes and their impacts

Between 1430 and 1605 UTC, the P-3 aircraft performed a flux stack just ahead of the secondary cold front about 140 km south of the coastline, as described in section 3 (see Figs. 5a and 7). This flux stack consisted of five level aircraft passes (or legs) approximately perpendicular to the frontal orientation and the low-level winds (Fig. 5a). The mean values of standard meteorological parameters in the warm sector are given in Table 1. The SSTs in the first two rows are obtained from measurements from an AXBT dropped in the warm sector from the leg at 427 m and from a downward-looking PRT-5 averaged along the lowest leg, respectively. The two measurements of 15.73° and 15.8°C are in excellent agreement with each other and with the AVHRR SST analysis of 15.5°–16.0°C (see Fig. 2). Estimates of the surface pressure from airborne measurements along the lowest flight leg are also presented. The computation of the surface mixing ratio includes the salinity effect of depressing the sea surface humidity by 2% compared to that of pure water (e.g., Fairall et al. 2003).

a. Flux measurements

In addition to the standard 1-s flight-level measurements, data were also collected at 40 Hz in order to observe turbulent structures down to a scale of about 5 m. Using data from the gust probe, fast thermistor, and Lyman-alpha hygrometer mounted on the aircraft, fluxes of sensible (H_s) and latent (H_l) heat and stress (τ) were calculated with the covariance technique along each leg (e.g., Friehe et al. 1986; Friehe and Khelif 1992; Khelif et al. 1999) and are presented in Table 1. To obtain a scalar flux accuracy of 10%, measurements should be made along 60-km legs (100 times the boundary layer height) in homogeneous conditions to ensure adequate statistical sampling (Lenschow and Stankov 1986). However, because of the presence of the two frontal features, this was impossible, and the warm-sector legs were only about half the desired length. As a consequence, we estimate the flux measurements to have an error of 15%–30% or less [i.e., between the 10% error obtainable with 60-km legs and the 21%–

47% error obtained by Khelif et al. (1999) with 10-km legs].

In the offshore warm sector, the H_l and H_s along the lowest leg are 32.1 and 12.1 W m^{-2}, respectively (Table 1). The H_l is positive along all legs but is a maximum at 427 m (113.6 W m^{-2}), and H_s is weak or negative at all altitudes above the lowest one. The stress becomes slightly negative above 590 m. The boundary layer depth is approximately 600 m, since above 590 m the vertical gradient of virtual potential temperature (θ_v) increases more rapidly, the specific humidity (q) decreases more rapidly, and the sign of the stress reverses. The wind speed is also a maximum near 600 m. Hence, the surface layer, where the fluxes should be approximately constant with height and which is often taken to be one-tenth of the boundary layer depth (e.g., Garratt 1992), is only about 60 m deep. The lowest flux leg is near the top of this constant flux layer, implying that the fluxes below are the same as along this leg. The fluxes are not constant with height within the rest of the boundary layer, as can be seen in Table 1.

b. Downwind impact of fluxes

The effect of the surface fluxes on the boundary layer as it moves toward the coast was estimated by two methods. In the first method, we assume that the fluxes below 66 m are the same as at 66 m, and that the fluxes at the different heights remain constant in time as the air parcel translates toward the coast. The flux divergence for each layer then gives the change for that layer, and the average change of a parameter for the entire boundary layer is the layer-weighted mean of the changes over the depth of the boundary layer. The changes for each layer and for the entire boundary layer using this method are seen in Table 2 (indicated by "WM").

The second method assumes that the surface fluxes are given by those measured at 66 m, and that the fluxes are approximately zero at the top of the boundary layer at 600 m. Hence, the flux divergence and the mean change in the entire boundary layer can be calculated. These results are given as (L1) in Table 2. In method L1, we assume that the observed fluxes in the interior of the PBL are details not important for the boundary layer as a whole. Thus, with this method we compute the changes in temperature (ΔT) and mixing ratio (Δq) by

$$\Delta T = -\Delta t(H_{s\_zb} - H_{s\_0})/(\rho_a c_p \mathrm{zb}), \tag{1a}$$

$$\Delta \mathrm{q} = -\Delta t(H_{l\_zb} - H_{l\_0})/(\rho_a L_v \mathrm{zb}), \tag{1b}$$

where Δt (=2.5 h) is the time between offshore and nearshore measurements; H_{s_zb}, H_{l_zb} are the sensible and latent heat fluxes at the boundary layer top (=0 W m^{-2}); and H_{s_0}, H_{l_0} are the surface sensible and latent heat fluxes (assumed to be the same as H_s and H_l measured at 66 m in Table 1). The boundary layer depth (=600 m), air density, specific heat of air at constant pressure, and latent heat of vaporization are given by zb, ρ_a, c_p, and L_v, respectively. Both methods WM and L1 give nearly identical results for the specific humidity; that is, the boundary layer specific humidity increases by only about 0.16 g kg^{-1}. The temperature is expected to increase by either 0.15° or 0.31°C. The larger discrepancy between the methods for temperature is likely due to the significant role of downward sensible heat flux near the top of the boundary layer. Though the WM method is probably the more accurate, the L1 method is the one that represents the effects from surface fluxes and will, therefore, be the one used in the subsequent discussions.

TABLE 2. Warm-sector changes in specific humidity (Δq), temperature (ΔT), and equivalent potential temperature ($\Delta\theta_e$) based on observed fluxes for each layer and for the entire 600-m-deep boundary layer. For the entire boundary layer, results from the weighted-mean (WM) and the first layer (L1) methods are shown.

Height layer (m)	Mean height (m)	Δq [g kg^{-1} (2.5 h)$^{-1}$]	ΔT [K (2.5 h)$^{-1}$]	$\Delta\theta_e$ [K (2.5 h)$^{-1}$]
0–66	33	0.00	0.00	0.00
66–285	175.5	−0.14	0.63	0.33
285–427	356	−1.59	2.24	−1.88
427–590	508.5	2.18	−1.69	+4.04
590–1154	872	−0.17	−0.26	−0.77
0–600 (WM)	300	0.17	0.31	0.79
0–600 (L1)	300	0.16	0.15	0.62

The increases in Table 2 are small values and would only produce a 0.15–0.3- and 0.6–0.8-K increase in θ and θ_e, respectively. A shallower boundary layer would produce proportionally greater increases, but the data do not argue for this. However, the H_s and H_l should increase by about 8 and 25 W m^{-2} respectively (~67%) as the air approaches the shore, since the aircraft-sensed sea surface radiative temperature (not shown) and the AVHRR SST analysis (Fig. 2) both increase by about 0.5°C shoreward. After adding this increase in surface fluxes, an increase of ~1 K in θ_e is estimated to occur along the trajectory to the coast. Increases of 6 W m^{-2} in both H_{s_0} and H_{l_0} over those in Table 1 (50% and 20% increases, respectively) only produce an increase in $\Delta\theta_e$ of 0.17 K, so the results are not very sensitive to errors in the surface fluxes equal to or greater than the estimated flux errors given above.

The cross section in the Santa Barbara Channel shows that the maximum warm-sector θ_e just ahead of the secondary cold front is 317 K (Fig. 8a), a 1° increase from that measured with the same airborne instruments 2.5 h earlier and shown in Fig. 7a. The profiles of θ_e for the offshore flux stack, the nearshore extrapolation of the offshore profile, and the nearshore aircraft observations (Fig. 13) show this agreement more explicitly. Although this agreement may be fortuitous, the fact that the airborne verification data were obtained at the right time at the right location for the estimated landfall of the sampled upwind air parcel lends strong credence

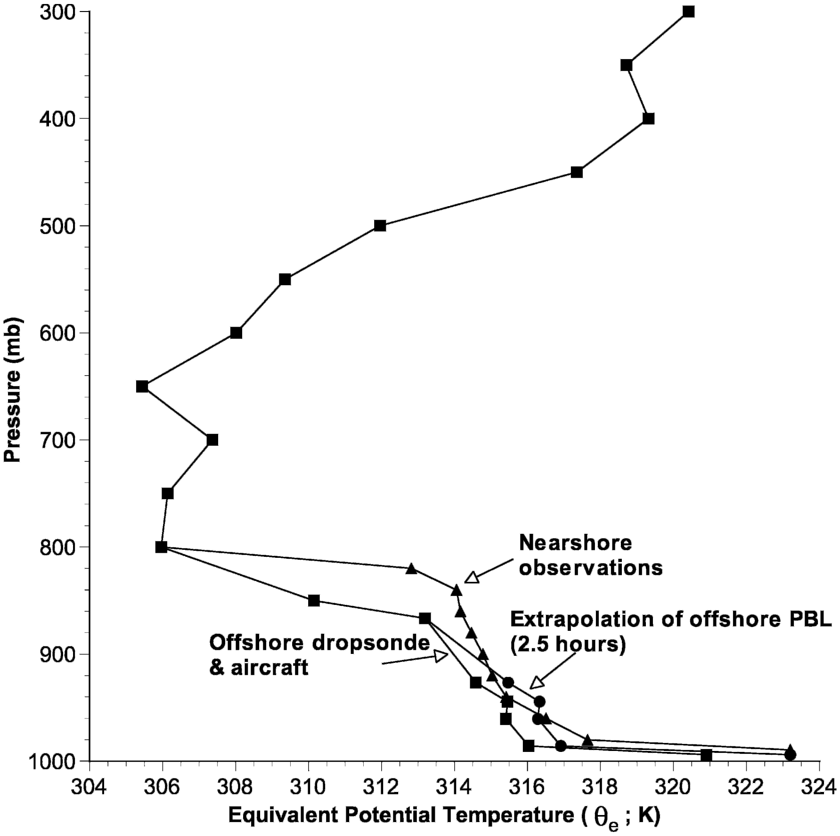

FIG. 13. Profiles of equivalent potential temperature (θ_e) for the offshore location (squares), extrapolation to the nearshore location using boundary layer changes due only to surface fluxes (dots), and nearshore observations (triangles). The offshore dropsonde data are used above the aircraft data for all profiles, i.e., above 867 mb for the offshore and extrapolated offshore profiles and above 820 mb for the observed nearshore profile. The 1200 UTC Vandenberg sounding is used above 500 mb.

to this result. Another perspective shows that the additional moisture added during this final 140-km transit to the coast over the warmer coastal water is only 1%–2% of the total water content of the air arriving at the coast. Hence, the direct moisture contribution to the coastal precipitation appears to be small.

However, the small amounts of warming and moistening of the lowest few hundred meters can make a larger impact on destabilizing the air being forced to ascend the front near the coast. To assess the impact of the surface fluxes on the stability, we compute the offshore CAPE by combining the low-level aircraft measurements (surface to 866 mb), the offshore 1356 UTC dropsonde (850 to 500 mb), and the 1200 UTC Vandenberg rawinsonde (500 to 300 mb) to obtain profile data to 300 mb. We then compute the nearshore CAPE by assuming that the only changes in the sounding occur in the boundary layer and are due to the surface fluxes (e.g., Fig. 13). CAPE is computed by

$$\mathrm{CAPE} = \int_{z_{\mathrm{LFC}}}^{z_{\mathrm{EQ}}} g\,(\theta_{\mathrm{v\_p}} - \theta_{\mathrm{v\_env}})/\theta_{\mathrm{v\_env}}\,dz, \qquad (2)$$

where $\theta_{\mathrm{v\_p}}$ and $\theta_{\mathrm{v\_env}}$ are the virtual potential temperatures of the lifted parcel and the environment, respectively, z_{LFC} and z_{EQ} are the levels of free convection and buoyant equilibrium, respectively, g is the acceleration due to gravity, and dz is the incremental height. CAPE can be computed from a parcel originating at just one height (such as the height that gives the maximum value) or averaged over a layer. Sometimes the CAPE of a surface-lifted parcel (SBCAPE) is used. Values of θ_e at the ocean surface are included in Fig. 13 for this purpose.

Regardless of whether one height or a layer is used or if the surface layer is included or not, the CAPE increases by 26%–31% from offshore to nearshore when the surface fluxes are used to moisten and warm the boundary layer (Table 3). A nearshore profile to 300 mb, reflecting primarily changes in the boundary layer, is obtained by using a profile based on aircraft data up to 820 mb obtained in the nearshore warm sector near 1652 UTC (see Figs. 5b and 8 for the location and Fig. 13 for the sounding) and the combined offshore dropsonde and Vandenberg rawinsonde aloft. The layer-

TABLE 3. Comparisons of CAPE (J kg^{-1}) calculations from the offshore profile, the offshore profile extrapolated to the nearshore location using the observed fluxes and method L1, and the nearshore observations. The first two columns show the mean CAPE over the two given layers, and the next two columns show the CAPE obtained using a parcel from the surface (SBCAPE) and from the atmospheric layer that gives the maximum CAPE (Max atm). The last column shows the range of CAPE increases from the offshore profile to the extrapolated or observed nearshore profiles of the four different CAPE estimates.

	Surface–940 mb	986–940 mb	Surface (SBCAPE)	Max atm	Increase
Offshore	391	318	1081	360 (986 mb)	—
Extrapolated	506	416	1360	461 (986 mb)	26%–31%
Nearshore	476	383	1356	521 (980 mb)	20%–45%

mean CAPEs for this nearshore profile are only slightly less than those obtained for the extrapolated offshore profile, again validating the extrapolated profile. Hence, the approximately 1-K increase of boundary layer θ_e increases the CAPE by about 26% from 391 to 491 J kg^{-1} (the average of the "extrapolated" and "nearshore" values), using the mean PBL CAPEs. The maximum atmospheric CAPE increases by 36%.

Though much smaller than Great Plains thunderstorm CAPEs, the CAPEs shown in Table 3 are in the upper half of CAPEs typical for cool-season, central California thunderstorms, for which the median SBCAPE is less than 500 J kg^{-1}, and the maximum SBCAPE is near 1300 J kg^{-1} (Monteverdi et al. 2003). No estimates of typical thunderstorm CAPE are available for the California south-coastal region, in which this event occurs.

The CAPE calculations using parcels within the surface-to-940-mb layer give a mean z_{LFC} of 1060 m for the offshore profile and 550 m for the nearshore one. This shows that 1) the slight warming and moistening of the boundary layer by the surface fluxes lowered the z_{LFC} for the lower part of the boundary layer, 2) the abrupt cold-frontal rise of 700 m estimated from Fig. 7 may be inadequate for the release of free convection offshore, as is suggested by the lack of convection at the offshore cross section evident in the NEXRAD data (Fig. 5a) and the offshore airborne radar data (not shown), and 3) the z_{LFC} is easily reached when the air is forced to ascend the 2-km-high leading edge of the secondary cold front in the nearshore area (see Figs. 8a and 11a). Though the height of the cold front at the coast would have been sufficient to initiate the convection even without the lowering of the z_{LFC}, both the shoreward lowering of the z_{LFC} and increase of the frontal depth apparently contributed to the offshore extent of the convection initiation. The CAPE calculations give z_{EQ} of between 5.5 and 6.5 km for the boundary layer parcels for both the offshore and nearshore profiles, showing that the surface fluxes do not produce deeper penetration of the convection for this case. The calculated z_{EQ} is in excellent agreement with the independent updraft top of 6.0–6.5 km obtained from the radar data (Fig. 11a), indicating that the "sounding" obtained by combining the three different data sources is likely not too different from reality. Because of the relatively weak buoyancy and low wintertime tropopause heights, equilibrium levels of California thunderstorms are typically between 4.5 and 10.6 km (Monteverdi et al. 2003).

The CAPE calculations and the associated changes in z_{LFC} show that the coastal surface fluxes significantly decrease the stability, thereby contributing to the offshore extent and intensity of the very heavy, but brief, precipitation observed at Goleta and elsewhere along this part of the California coast. Though the coastal surface fluxes are not the primary cause for the coastal convection, their significant contribution to the destabilization will produce a positive contribution to the convection. Because our assertion that a majority of the warm-sector boundary layer air remains at low levels to be modified by the surface fluxes during the entire transit to the coast is crucial to this thesis, this assertion is tested by a simulation of this case in the next section. However, a more detailed modeling study, which could assess the quantitative impact of a 26% increase in CAPE on the ensuing convection (e.g., on updraft velocity or precipitation intensity) and perform various sensitivity tests, is beyond the scope of this paper.

5. Numerical simulations

The analyses of numerical simulations for understanding observations are only useful if these simulations faithfully reproduce the observed structures and are able to represent the principal physical processes. A simulation with the fifth-generation Pennsylvania State University–National Center for Atmospheric Research Mesoscale Model (MM5) using initial and boundary conditions from the European Centre for Medium-Range Weather Forecasts (ECMWF) and the AVHRR SST analysis shown in Fig. 2 was able to reproduce the main features of the primary and secondary cold fronts of this case. Hence, we use this simulation to show that the trajectories estimated from the observations in section 3 and Fig. 9 are reasonable, and that the observed changes between the offshore and nearshore cross sections presented in section 4 are consistent with changes along trajectories.

The simulation used three grid domains with grid spacings of 36, 12, and 4 km, respectively. The Medium-Range Forecast Model (MRF) boundary layer scheme (Hong and Pan 1996) was used on all domains. The Grell convective scheme was used on the two coarse

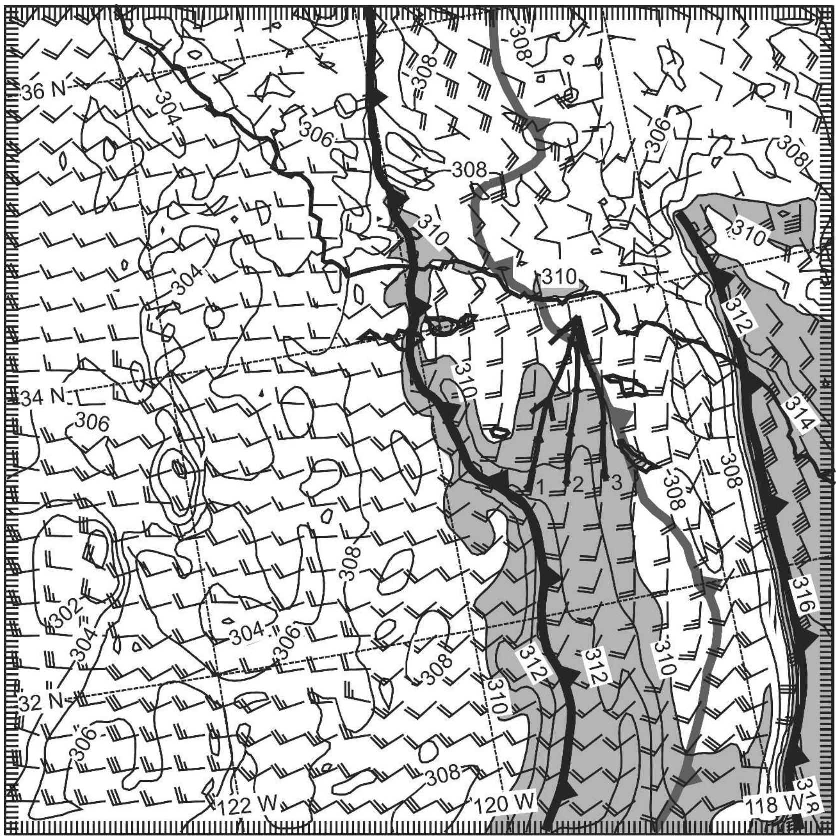

FIG. 14. MM5 output of θ_e (K; thin solid) and wind barbs (as in Fig. 2) at 950 mb at 1500 UTC 3 February 1998. Also shown are the primary and secondary cold fronts at 1500 UTC (dark heavy toothed lines), the secondary cold front at 1800 UTC (gray heavy toothed line), and trajectories T_1, T_2, and T_3 (arrowed moderate lines labeled 1, 2, and 3, respectively) starting at 200-m height in the warm sector at 1500 UTC and ending at 1800 UTC. Areas with θ_e greater than 310 K are shaded, and isopleths 311 and 313 K are added for clarity. Large arrows on the trajectories indicate a high height, while small arrows indicate a low height. See Fig. 15 for quantitative values along the trajectories.

domains, while an explicit microphysics scheme using "simple ice" was used on the finest domain (Grell et al. 1994). Fifty vertical layers were used, with 12 layers below about 1500-m altitude. The simulation was initialized at 0000 UTC 2 February and run for 48 h, so output at 1500 UTC on 3 February represents a 39-h forecast. The 4-km domain was only used between 1300 and 1800 UTC on 3 February. Model output data were extracted every 15 min on the finest domain to obtain trajectories with a satisfactory temporal resolution.

The simulation produced a secondary front very close to the observed secondary-front location at 1500 UTC 3 February (cf. Fig. 14 with Fig. 5a), though the simulated primary front was located too far to the east. The simulated low-level θ_e and wind fields, which included a weak warm-sector LLJ (note the three 15 m s^{-1} wind flags near the trajectories in Fig. 14), clearly showed this secondary front, including its NNW–SSE orientation. However, the simulation did have some erroneous features, such as θ_e values in the warm-sector air ahead of the secondary front that were about 3–5 K too low (cf. Fig. 14 with Fig. 7a) and low-level winds that were about 5 m s^{-1} too weak and with a slightly too strong westerly component (cf. Fig. 14 with Fig. 5a). Precipitation was produced along the secondary cold front over and north of the Channel Islands and over the Santa Ynez Mountains (not shown), but not south of the Channel Islands until after 1700 UTC contrary to that observed (see Fig. 5). The precipitation intensities were about 50%–70% of those observed, consistent with the lower values of θ_e. Despite the differences in these details, the simulation successfully reproduced the observed general structure and timing of this secondary front.

Trajectories T_1, T_2, and T_3, released in the warm sector ahead of the simulated secondary cold front, stay just to the warm-sector side of the secondary cold front all the way to the coast at 1800 UTC as shown in Fig. 14, with the convergence of the trajectories indicating confluent airflow in the warm sector. This is in good accord

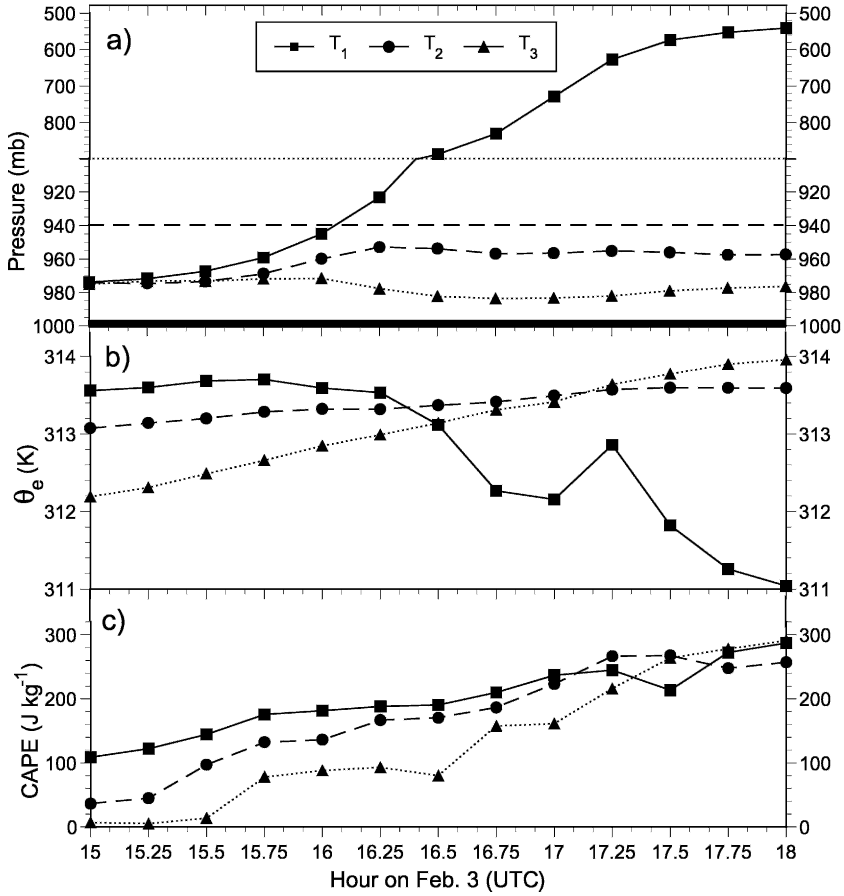

FIG. 15. Time series of (a) pressure (mb), (b) θ_e (K), and (c) column-maximum CAPE (J kg^{-1}) along the three trajectories T_1 (squares), T_2 (dots), and T_3 (triangles) shown in Fig. 14 for the MM5 simulation. The dashed line in (a) represents the approximate top of the observed boundary layer. To clearly show the vertical range of all three trajectories, the scale of the y axis in (a) was changed at the dotted line near 900 mb.

with the results described in section 3. However, because of the above differences, the trajectories moved slightly slower and slightly farther to the east than suggested by the observations and Fig. 9, and were cooler and drier (principally drier) than the observations. In the vertical, trajectories T_2 and T_3 remain within the boundary layer while T_1 is lifted by the front about halfway to the coast (Fig. 15a). This is precisely the scenario estimated in section 3 by using the differential velocities of the warm-sector air and the secondary cold front. Furthermore, the increases in θ_e along the trajectories remaining in the PBL (T_2 and T_3) are 0.6 and 1.7 K, respectively (Fig. 15b), which are very similar to the 1-K change estimated in section 4. Finally, the increases in CAPE along the trajectories ranged between 175 and 280 J kg^{-1}, slightly higher than the 101–161 J kg^{-1} increases estimated in Table 3. The CAPE values along the trajectories were calculated from the layer with the greatest θ_e in the atmospheric column, producing CAPE values corresponding to the "Max atm" column in Table 3. Hence, this simulation clearly demonstrates that at least half of the warm-sector PBL air at the offshore location remained at low levels within the warm sector on its approximate 3-h transit to the coast, and that the surface fluxes along this transit produced changes in θ_e and CAPE consistent with the observed changes. This supports our claim that the observed changes in θ_e and CAPE were caused by the surface fluxes within about 150 km of the coastline. Note also that both the coastal CAPE and precipitation values in the simulation are less than those observed, consistent with their assumed relationship.

6. Climatological relationship

a. *Extension to non–El Niño years*

The above results suggest that coastal surface fluxes contributed to the heavy coastal precipitation for this event occurring during an El Niño winter. However, what do these results suggest for the influence of coastal fluxes during non–El Niño years? To examine

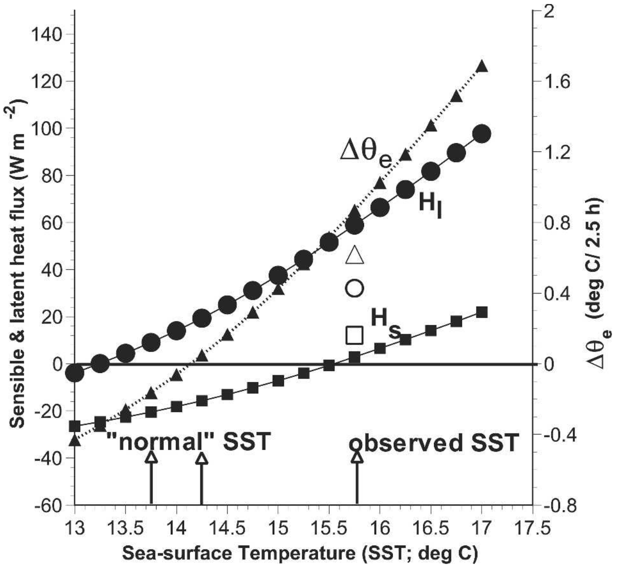

FIG. 16. Sensible heat flux (H_s; solid squares), latent heat flux (H_l; solid circles), and associated 2.5-h change in the boundary layer θ_e ($\Delta\theta_e$; solid triangles) as a function of SST. The computations of H_s, H_l, and $\Delta\theta_e$ were done using the bulk algorithm of Fairall et al. (2003) and assuming conditions as observed in the offshore warm sector on 3 Feb (given by the flight leg at 66 m in Table 1, and with PBL height = 600 m). Also shown are the observed covariance H_s (open square), H_l (open circle), and $\Delta\theta_e$ (open triangle). The observed SST and the range from more normal years are marked by arrows along the bottom.

this question, we utilized the Coupled Ocean–Atmosphere Response Experiment (COARE 3.0) surface flux parameterizations of Fairall et al. (1996, 2003) to compute the surface H_s and H_l for a range of SSTs that included both the observed El Niño values and values typical for non–El Niño years (Fig. 16). In these computations, we assume that the boundary layer conditions were the same as that observed for the 3 February case. The expected 2.5-h changes in boundary layer air temperature, mixing ratio, and θ_e are then computed.

The results for the observed El Niño conditions show that the parameterization does a reasonable job at predicting the observed surface fluxes and the change in boundary layer θ_e (Fig. 16). The discrepancies may be as much due to the limited sampling distance for the observed fluxes (i.e., see section 4a) as to any failure in the COARE 3.0 scheme. Hence, the model appears reliable. For SSTs 1.5°–2.0°C cooler than those observed, representative of non–El Niño years, the H_s was substantially negative (-15 to -20 W m^{-2}) and the H_l was positive (10–22 W m^{-2}) but smaller. Hence, the change in θ_e is predicted to be near zero or slightly negative. That is, the coastal surface fluxes are not expected to contribute to the destabilization of the boundary layer during landfalling storms in a non–El Niño year, even though they do contribute during El Niño years. They might even lead to slight stabilization.

b. Relation to studies of ENSO effects

Precipitation in coastal California is generally enhanced during the strong type 1 El Niño episodes (Fu et al. 1986), of which the winter 1997/98 was one. Precipitation amounts in southern California are typically 160%–185% of normal, with smaller enhancements in northern California (Schoner and Nicholson 1989; Redmond and Koch 1991). Furthermore, the frequency of daily precipitation events that exceeded the 90th percentile precipitation amount is greatly enhanced in coastal southern California during the warm ENSO phases as compared to the cold ones (Cayan et al. 1999), likely resulting in the significantly larger floods during El Niño compared to non–El Niño episodes (Andrews et al. 2004). This increase in the frequency of the heavy precipitation and extreme flooding events also diminishes northward. In the southern California coastal region, the El Niño of 1997/98 produced the second wettest January–March period compared to the 10 strongest El Niño years since 1915 (Barnston et al. 1999).

The main physical mechanisms for this increase in precipitation are generally known. During El Niño winters, enhanced convection in the eastern tropical Pacific produces an anomalous upper-tropospheric ridge in the subtropics and an enhanced Hadley circulation. At the same time, the Aleutian low strengthens and moves southwestward, producing anomalous troughing in the central Pacific. This leads to the formation of a stronger than normal subtropical jet stream and a southern storm track in the central and eastern Pacific, entering the United States in California and crossing the southern part of the country (Horel and Wallace 1981; Barnston and Livezey 1987; Shukla 1998; Barnston et al. 1999). Hence, stronger storms and more frequent storms can affect southern and central California.

Previous studies of the impact of the ENSO-generated SST anomalies in the North Pacific Ocean have focused on their feedback on the extratropical atmospheric structure and circulation, rather than on the precipitation distribution. These studies have utilized GCMs with grid spacings of 225–450 km and one-dimensional ocean mixed-layer representations. A recent review by Alexander et al. (2002) discusses and explains some of the initial contradictory results (Alexander 1992; Lau and Nath 1996; Lau 1997; Bladé 1999; Lau and Nath 2001), presents some new analyses, and concludes that the ENSO-generated SST anomalies weakly damp the direct atmospheric response to ENSO in the eastern half of the North Pacific Ocean during an El Niño winter. That is, the ENSO-generated negative longwave 500-mb height anomalies are smaller in magnitude when the ENSO-generated SST anomalies, dominated by the negative SST anomalies in the central North Pacific Ocean, are allowed to interact with the atmospheric circulation than when they are not. However, none of these studies are sufficiently detailed to suggest how the ENSO-produced SST anomalies, including the warm anomalies along the California coast, affect the storm tracks or individual storms. Studies using mesoscale models in combination with El Niño–modified SST distributions are needed to reveal whether the process operating in our case study is a positive feedback for climatological precipitation enhancement during a warm ENSO event.

The ENSO-modulated physical mechanism presented in this study appears therefore not to have been previously considered. Through an enhancement of CAPE during pre-cold-frontal onshore flow, this mechanism links the generation of anomalously warm SSTs along the California coast to small but potentially significant enhancements in the coastal cold-frontal precipitation from each storm, thereby adding to the ENSO-enhanced precipitation in that region. Such enhancements to the CAPE will be most effective for enhancing the precipitation in flow where some CAPE already exists. This study suggests this will tend to be in the warm-sector regions of the storms in coastal southern California, where the storm systems are less likely to be occluded and the SSTs are warmer, though convection in cold-core postfrontal situations might also be enhanced. In non–El Niño years, when the coastal SSTs are 1.5°–3°C colder, the surface heat fluxes will not enhance the CAPE and may even suppress it. This result assumes that the thermodynamic structure in the boundary layer of the non–El Niño storms is similar to that in storms during an El Niño year. If the boundary layer air is colder in storms in a non–El Niño year at a given location along the coast, then the coastal surface fluxes could still enhance the CAPE. Furthermore, the results obtained for this El Niño–year storm may not represent other storms during El Niño years. This case was chosen because of the available measurements and the presence of the convection, and only serves as a suggestion that this process may contribute to coastal precipitation. Studies using more cases and producing boundary layer mean states for El Niño and non–El Niño years are necessary to assess the climatological importance of this process, but such tasks are beyond the scope of this study.

Reed and Blier (1986a,b) examine two 1982 cold-core systems that were very similar to each other over the open ocean but produced different effects on landfall in the California Bight. The storm in March 1982 produced mainly moderate stratiform precipitation as it made landfall, while the one in November 1982 produced severe convection with heavy precipitation and tornadoes. Near-normal SSTs existed in March 1982 in the California Bight, but the strong ENSO event of 1982/83 had produced positive SST anomalies of 0.5°–0.75°C by November 1982 (NOAA/Climate Diagnostic Center database). This El Niño effect combined with the seasonal variation of SST accounted for the 3°C SST difference between the March and November 1982 cases. Though detailed observations of the 1982 storms do not exist to determine the reasons for the differences in the character of the precipitation and to examine the role of coastal surface fluxes, the more severe convection with the November storm compared to the March storm is consistent with our hypothesis of influences of the SSTs within 150 km of the shore on the coastal precipitation in southern California and with the role of ENSO as a regulator of those SSTs. Though the connection is speculative, these cases provide specific examples of how the El Niño modulation of the coastal SST anomalies may impact individual storms and thereby the coastal climate.

7. Conclusions

This paper uses extensive measurements near a secondary cold front on 3 February 1998 in the California Bight to assess the contribution of surface sensible and latent heat fluxes within 150 km of the shore to the significant coastal precipitation. The observed nearshore, warm-sector, thermodynamic structure is in excellent agreement with the observed offshore warm-sector structure upstream, once modifications by the observed surface fluxes are included. Furthermore, a simulation with the MM5 shows that these modifications are quantitatively consistent with changes occurring along boundary layer trajectories in the simulated warm sector. These modifications show that the direct contribution of heat and moisture to the warm sector increases θ_e by only about 1 K, and is therefore small. However, the observed fluxes do increase the CAPE by ~26%, thereby contributing significantly to the destabilization of the air before it is forced to ascend at the cold front where it intersects the steep coastal terrain. As the air ascends, deep convection occurs with coastal flooding as a result. This process is shown schematically in Fig. 17. In cases where the shoreward flow is not in the vicinity of a front, the lifting is done by the coastal terrain, but the updrafts will still be enhanced by the nearshore coastal fluxes if saturation is realized.

A bulk surface flux parameterization is shown to match direct surface flux measurements reasonably well in this case. It is used to extend the results to suggest that the coastal fluxes during pre-cold-frontal onshore flow only enhance the coastal precipitation during years with anomalously warm coastal sea surface temperatures (ENSO years), such as 1998, and may even help suppress coastal convection during years of more normal colder coastal SSTs.

Though this is only one case and the effect of surface fluxes vary from storm to storm, these results serve to illustrate a point. During El Niño years when coastal waters are anomalously warm by 1.5°–2.5°C, surface heat fluxes near the California coast can contribute significantly to the coastal precipitation. During non–El Niño years, they are much less likely to do so unless the air temperatures in the storms are correspondingly

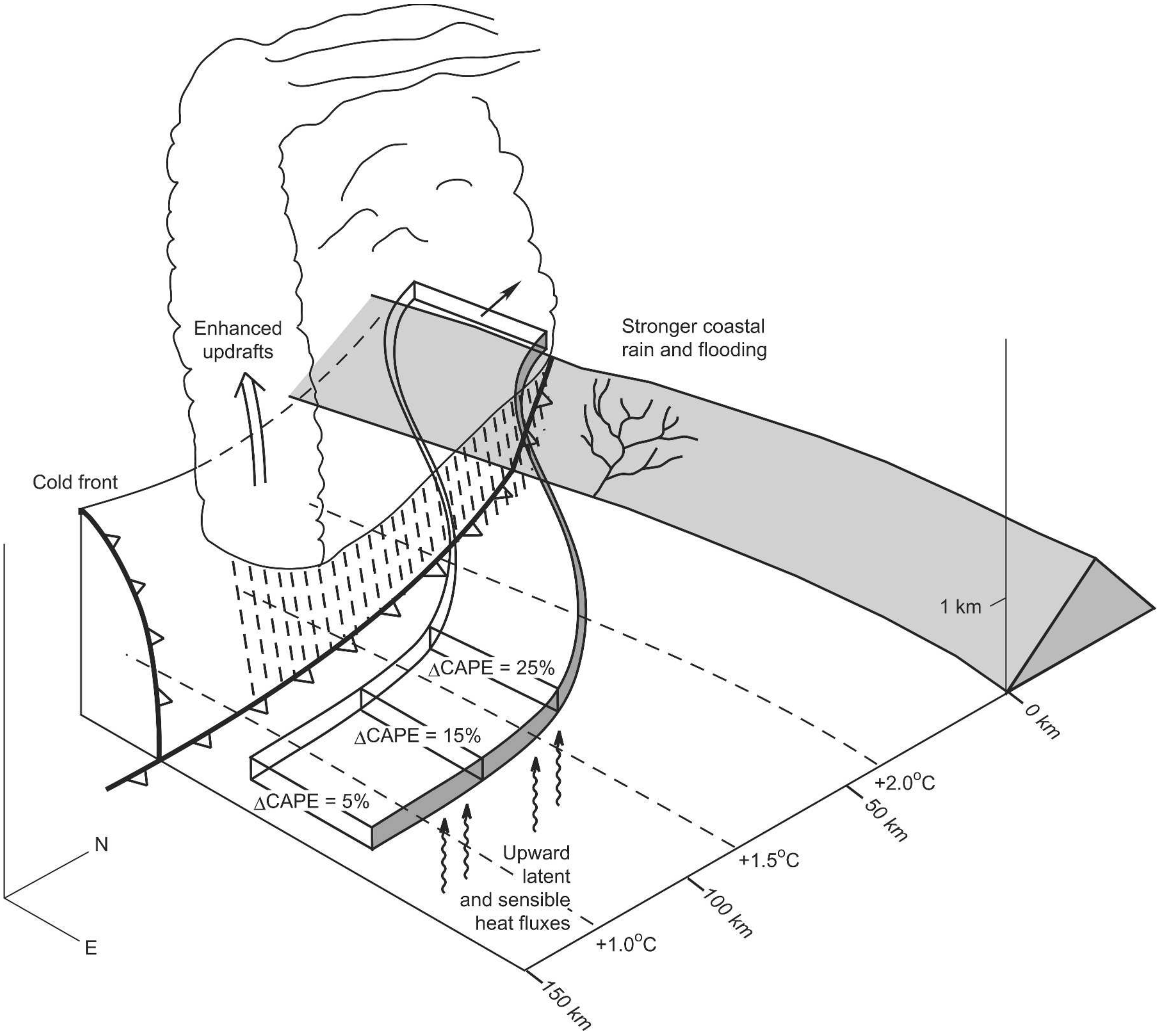

FIG. 17. Schematic showing the effect of the nearshore surface fluxes (wavy arrows) on the low-level stability (CAPE) and frontal updrafts as the front-parallel, low-level jet flow (flat ribbon) is lifted by the front as it approaches the coast. The toothed heavy lines depict the cold-frontal surface, and the dashed lines show the SST anomaly (°C). A small drainage basin is shown on the sloping terrain (gray shaded).

colder. Though this study indicates that this process could be a positive feedback of ENSO changes important for coastal precipitation and heavy precipitation events, future studies using more cases or higher-resolution climate models are necessary to establish its climatological importance.

Acknowledgments. The CALJET field program was made possible by the dedicated participation of many individuals representing numerous organizations. We are grateful to all of them. We particularly recognize the dedication of the crew of the NOAA WP-3D aircraft in collecting a huge dataset with minimum rest during the busy 1998 El Niño storm season, and the staff of the Naval Postgraduate School who hosted the CALJET operations center. We also appreciate the work of Sean Burns in processing the P-3 turbulent flux data, David White in processing the airborne radar data, and Sara Michelson for her assistance in running the MM5. Thoughtful comments by two anonymous reviewers led to an improved manuscript. The original data collection during CALJET was sponsored by several programs, including NOAA's El Niño Rapid Response Program and the U.S. Weather Research Program. This analysis work was supported by NOAA Grant NA77RJ0453 through the University of California, San Diego, and NOAA's Weather–Climate Connection Program.

REFERENCES

Alexander, M. A., 1990: Simulation of the response of the North Pacific Ocean to the anomalous atmospheric circulation associated with El Niño. *Climate Dyn.,* **5,** 53–65.

——, 1992: Midlatitude atmosphere-ocean interaction during El Niño. Part I: The North Pacific Ocean. *J. Climate,* **5,** 944–958.

——, I. Bladé, M. Newman, J. R. Lanzante, N.-C. Lau, and J. D. Scott, 2002: The Atmospheric Bridge: The influence of ENSO teleconnections on air-sea interactions over the global oceans. *J. Climate,* **15,** 2205–2231.

Andrews, E. D., R. C. Antweiler, P. J. Neiman, and F. M. Ralph, 2004: Influence of ENSO on flood frequency along the California coast. *J. Climate*, **17,** 337–348.

Barnston, A. G., and R. E. Livezey, 1987: Classification, seasonality and persistence of low-frequency atmospheric circulation patterns. *Mon. Wea. Rev.,* **115,** 1083–1126.

——, A. Leetma, V. E. Kousky, R. E. Livezey, E. A. O'Lenic, H. Van den Dool, A. J. Wagner, and D. A. Unger, 1999: NCEP forecasts of the El Niño of 1997–98 and its U.S. impacts. *Bull. Amer. Meteor. Soc.,* **80,** 1829–1852.

Bjerknes, J., and H. Solberg, 1921: Meteorological conditions for the formation of rain. *Geofys. Publ.,* **2,** 10–41.

Bladé, I., 1999: The influence of midlatitude ocean–atmosphere coupling on the low-frequency variability of a GCM. Part II: Interannual variability induced by tropical SST forcing. *J. Climate,* **12,** 21–45.

Bolton, D., 1980: Computation of equivalent potential temperature. *Mon. Wea. Rev.,* **108,** 1046–1053.

Cayan, D. R., K. T. Redmond, and L. G. Riddle, 1999: ENSO and hydrologic extremes in the western United States. *J. Climate,* **12,** 2881–2893.

Doyle, J. D., 1997: The influence of mesoscale orography on a coastal jet and rainband. *Mon. Wea. Rev.,* **125,** 1465–1488.

Fairall, C. W., E. F. Bradley, J. E. Hare, A. A. Grachev, and J. B. Edson, 2003: Bulk parameterization of air–sea fluxes: Updates and verification for the COARE algorithm. *J. Climate,* **16,** 571–591.

——, ——, D. P. Rogers, J. B. Edson, and G. S. Young, 1996: Bulk parameterization of air–sea fluxes for Tropical Ocean–Global Atmosphere Coupled-Ocean Atmosphere Response Experiment. *J. Geophys. Res.,* **101,** 3747–3764.

Friehe, C. A., and D. Khelif, 1992: Fast-response aircraft temperature sensors. *J. Atmos. Oceanic Technol.,* **9,** 784–795.

——, R. L. Grossman, and Y. Pann, 1986: Calibration of an airborne Lyman-alpha hygrometer and measurement of water vapor flux using a thermoelectric hygrometer. *J. Atmos. Oceanic Technol.,* **3,** 299–304.

Fu, C., H. F. Diaz, and J. O. Fletcher, 1986: Characteristics of the responses of SST in the central Pacific associated with warm episodes of the Southern Oscillation. *Mon. Wea. Rev.,* **114,** 1716–1738.

Garner, S. T., 1999: Blocking and frontogenesis by two-dimensional terrain in baroclinic flow. Part I: Numerical experiments. *J. Atmos. Sci.,* **56,** 1495–1508.

Garratt, J. R., 1992: *The Atmospheric Boundary Layer*. Cambridge University Press, 316 pp.

Giordani, H., and G. Caniaux, 2001: Sensitivity of cyclogenesis to sea surface temperature in the northwest Atlantic. *Mon. Wea. Rev.,* **129,** 1273–1295.

Grell, G. A., J. Dudhia, and D. R. Stauffer, 1994: A description of the fifth-generation Penn State/NCAR Mesoscale Model (MM5). NCAR Tech. Note NCAR/TN-398 + STR, 138 pp. [Available online at http://www.mmm.ucar.edu/mm5/doc1.html.]

Gyakum, J. R., and R. E. Danielson, 2000: Analysis of meteorological precursors to ordinary and explosive cyclogenesis in the western North Pacific. *Mon. Wea. Rev.,* **128,** 851–863.

Hobbs, P. V., and P. O. G. Persson, 1982: The mesoscale and microscale structure and organization of clouds and precipitation in midlatitude cyclones. Part V: The substructure of narrow cold-frontal rainbands. *J. Atmos. Sci.,* **39,** 280–295.

Hong, S.-Y., and H.-L. Pan, 1996: Nonlocal boundary layer vertical diffusion in a medium-range forecast model. *Mon. Wea. Rev.,* **124,** 2322–2339.

Horel, J. D., and J. M. Wallace, 1981: Planetary-scale atmospheric phenomena associated with the Southern Oscillation. *Mon. Wea. Rev.,* **109,** 813–829.

Jorgensen, D. P., P. H. Hildebrand, and C. L. Frush, 1983: Feasibility test of an airborne pulse-Doppler meteorological radar. *J. Climate Appl. Meteor.,* **22,** 744–757.

——, T. Matejka, and J. D. DuGranrut, 1996: Multi-beam techniques for deriving wind fields from airborne Doppler radars. *Meteor. Atmos. Phys.,* **59,** 83–104.

——, Z. Pu, P. O. G. Persson, and W.-K. Tao, 2003: Variations associated with cores and gaps of a Pacific narrow cold frontal rainband. *Mon. Wea. Rev*., **131,** 2705–2729.

Khelif, D., S. P. Burns, and C. A. Friehe, 1999: Improved wind measurements on research aircraft. *J. Atmos. Oceanic Technol.,* **16,** 860–875.

Kristjánsson, J. E., and S. Thorsteinsson, 1995: The structure and evolution of an explosive cyclone near Iceland. *Tellus,* **47A,** 656–670.

Kuo, Y.-H., and R. J. Reed, 1988: Numerical simulation of an explosively deepening cyclone in the eastern Pacific. *Mon. Wea. Rev.,* **116,** 2081–2105.

——, ——, and S. Low-Nam, 1991: Effects of surface energy fluxes during the early development and rapid intensification stages of seven explosive cyclones in the western Atlantic. *Mon. Wea. Rev.,* **119,** 457–476.

Langland, R. H., R. L. Elsberry, and R. M. Errico, 1995: Evaluation of physical processes in an idealized extratropical cyclone using adjoint techniques. *Quart. J. Roy. Meteor. Soc.,* **121,** 1349–1386.

Lau, N.-C., 1997: Interactions between the global SST anomalies and the midlatitude atmospheric circulation. *Bull. Amer. Meteor. Soc.,* **78,** 21–33.

——, and M. J. Nath, 1996: The role of the "atmospheric bridge" in linking tropical Pacific ENSO events to extratropical SST anomalies. *J. Climate,* **9,** 2036–2057.

——, and ——, 2001: Impact of ENSO on SST variability in the North Pacific and North Atlantic: Seasonal dependence and role of extratropical sea–air coupling. *J. Climate,* **14,** 2846–2866.

Lenschow, D. H., and B. B. Stankov, 1986: Length scales in the convective boundary layer. *J. Atmos. Sci.,* **43,** 1198–1209.

Monteverdi, J. P., C. A. Doswell III, and G. S. Lipari, 2003: Shear parameter thresholds for forecasting tornadic thunderstorms in northern and central California. *Wea. Forecasting,* **18,** 357–370.

Namias, J., and D. R. Cayan, 1981: Large-scale air–sea interactions and short period climate fluctuations. *Science,* **214,** 869–876.

Neiman, P. J., P. O. G. Persson, F. M. Ralph, D. P. Jorgensen, A. B. White, and D. E. Kingsmill, 2004: Modification of fronts and precipitation by coastal blocking during an intense landfalling winter storm in southern California: Observations during CALJET. *Mon. Wea. Rev.,* **132,** 242–273.

——, F. M. Ralph, A. B. White, D. A. Kingsmill, and P. O. G. Persson, 2002: The statistical relationship between upslope flow and rainfall in California's coastal mountains: Observations during CALJET. *Mon. Wea. Rev.,* **130,** 1468–1492.

Parsons, D. B., 1992: An explanation of intense frontal updrafts and narrow cold-frontal rainbands. *J. Atmos. Sci.,* **49,** 1810–1825.

Persson, P. O. G., F. M. Ralph, B. Walter, P. Neiman, C. King, A. White, and J. Wilczak, 1999: Observations of the structure of the low-level jet in landfalling winter storms using the CALJET observational network. Preprints, *Third Symp. on Integrated Observing Systems*, Dallas, TX, Amer. Meteor. Soc., 82–85.

Ralph, F. M., and Coauthors, 1999: The California Land-falling Jets Experiment (CALJET): Objectives and design of a coastal atmosphere–ocean observing system deployed during a strong El Niño. Preprints, *Third Symp. on Integrated Observing Systems*, Dallas, TX, Amer. Meteor. Soc., 78–81.

——, P. J. Neiman, D. E. Kingsmill, P. O. G. Persson, A. B. White, E. T. Strem, E. D. Andrews, and R. C. Antweiler, 2003: The impact of a prominent rain shadow on flooding in California's Santa Cruz Mountains: A CALJET case study and sensitivity to the ENSO cycle. *J. Hydrometeor,* **4,** 1243–1264.

Redmond, K. T., and R. W. Koch, 1991: Surface climate and streamflow variability in the western United States and their relationship to large-scale circulation indices. *Water Resour. Res.,* **27,** 2381–2399.

Reed, R. J., and M. D. Albright, 1986: A case study of explosive cyclogenesis in the eastern Pacific. *Mon. Wea. Rev.,* **114,** 2297–2319.

——, and W. Blier, 1986a: A case study of comma cloud development in the eastern Pacific. *Mon. Wea. Rev.,* **114,** 1681–1695.

——, and ——, 1986b: A further study of comma cloud development in the eastern Pacific. *Mon. Wea. Rev.,* **114,** 1696–1708.

——, and A. J. Simmons, 1991: An explosively deepening cyclone over the North Atlantic that was unaffected by concurrent surface energy fluxes. *Wea. Forecasting,* **6,** 117–122.

Schoner, T., and S. E. Nicholson, 1989: The relationship between California rainfall and ENSO events. *J. Climate,* **2,** 1258–1269.

Shukla, J., 1998: Predictability in the midst of chaos: A scientific basis for climate forecasting. *Science,* **282,** 728–731.

Wakimoto, R., and B. L. Bosart, 2000: Airborne radar observations of a cold front during FASTEX. *Mon. Wea. Rev.,* **128,** 2447–2470.

Wernli, H., 1997: A Lagrangian-based analysis of extratropical cyclones. II: A detailed case-study. *Quart. J. Roy. Meteor. Soc.,* **123,** 1677–1706.

Wuertz, D. B., B. L. Weber, R. G. Staruch, A. S. Frisch, C. G. Little, D. A. Merritt, K. P. Moran, and D. C. Welsh, 1988: Effects of precipitation on UHF wind profiler measurements. *J. Atmos. Oceanic Technol.,* **5,** 450–465.

Yu, C.-K., and N. A. Bond, 2002: Airborne Doppler observations of a cold front in the vicinity of Vancouver Island. *Mon. Wea. Rev.,* **130,** 2692–2708.

Zhang, D.-L., E. Radeva, and J. Gyakum, 1999: A family of frontal cyclones over the western Atlantic Ocean. Part II: Parameter studies. *Mon. Wea. Rev.,* **127,** 1745–1760.